Characteristics of Kelvin-Helmholtz Waves as Observed by the MMS from September 2015 to March 2020

Rachel Rice[1], **Katariina Nykyri**[1], **Xuanye Ma**[1], **Brandon Burkholder**[1]

[1]Embry-Riddle Aeronautical University, Department of Physical Sciences, Center for Space and Atmospheric Research

Key Points:

- A survey of MMS data from September 2015 to March 2020 identified 50 Kelvin-Helmholtz wave events.
- Events are typically observed for solar wind speed between 295−610 km/s. Growth rates are otherwise independent of solar wind conditions.
- A new method is developed for the automatic detection of magnetosheath and magnetospheric regions within the KHI.

Corresponding author: Rachel Rice, `ricer4@my.erau.edu`

Abstract

The Magnetospheric Multiscale (MMS) mission has presented a new opportunity to study the fine scale structures and phenomena of the Earth's magnetosphere, including cross scale processes associated with the Kelvin-Helmholtz Instability (KHI), but such studies of the KHI and its secondary processes will require a database of MMS encounters with KH waves. Here we present an overview of 50 MMS observations of the KHI from September 2015 to March 2020. Growth rates and unstable solid angles for each of the 50 events were calculated using a new technique to automatically detect plasma regions on either side of the magnetopause boundary. There was no apparent correlation between solar wind conditions during the KHI and its growth rate and unstable solid angle, which is not surprising as KH waves were observed downstream of their source region. We note most KHI were observed for solar wind flow speeds between 295 km/s and 610 km/s, likely due to a filtering effect of the instability onset criteria and plasma compressibility. Two-dimensional Magnetohydrodynamic (2D MHD) simulations were compared with two of the observed MMS events. Comparison of the observations with the 2D MHD simulations indicates that the new region sorting method is reliable and robust. The ability to automatically detect separate plasma regions on either side of a moving boundary and determine the KHI growth rate may prove useful for future work identifying and studying secondary processes associated with the KHI.

1 Introduction

The ways in which the solar wind (SW) couples to the Earth's magnetosphere and its impacts on local space weather is a fundamental question of space physics. Several mechanisms operating at the magnetopause boundary, such as magnetic reconnection [*Paschmann et al.*, 1979; *Sonnerup et al.*, 1981; *Gosling et al.*, 1986; *Burch and Phan*, 2016] and viscous interactions [*Axford and Hines*, 1961; *Otto and Fairfield*, 2000; *Fairfield et al.*, 2000], are responsible for the transfer of mass and energy from the solar wind to the magnetosphere. Understanding the detailed effects of these processes is vital to predict and help prevent negative outcomes from space weather. Consider as an example, the dawn-dusk asymmetry of the magnetosphere plasma sheet.

Observations from Defense Meteorological Satellite Program (DMSP) and Time History of Events and Macroscale Interactions during Substorm (THEMIS) spacecraft have established that the cold component ions of the plasma sheet are 30-40% hotter in the dawn flank than in the dusk [*Hasegawa et al.*, 2003; *Wing et al.*, 2005; *Dimmock et al.*, 2015]. *Dimmock et al.* [2015] conducted a statistical study of the magnetosheath source population as observed by THEMIS spacecraft over seven years, which showed ions in the dawn flank are on average 10-15% hotter than those in the dusk flank. This asymmetry is more pronounced under fast (> 400 km/s) SW conditions [*Dimmock et al.*, 2015]. However, even during fast SW, the asymmetry of the magnetosheath source plasma is insufficient to produce the observed asymmetry in the plasma sheet. MHD simulations were unable to reproduce the observed sheath asymmetry, but it was apparent in hybrid models, suggesting a kinetic scale mechanism is responsible for asymmetrically driving the heating of cold component ions in the sheath [*Dimmock et al.*, 2015].

Several physical mechanisms have been proposed as drivers of the observed plasma sheet asymmetry. The Kelvin-Helmholtz instability (KHI), which occurs regularly at the magnetopause boundary, is one such mechanism [*Otto and Fairfield*, 2000; *Fairfield et al.*, 2000; *Nykyri et al.*, 2003; *Hasegawa et al.*, 2004; *Nykyri et al.*, 2006; *Taylor et al.*, 2008; *Foullon et al.*, 2008; *Merkin et al.*, 2013; *Lin et al.*, 2014; *Ma et al.*, 2014a,b; *Nykyri et al.*, 2017; *Ma et al.*, 2017; *Sorathia et al.*, 2019]. The KHI occurs in regions of large shear flow [*Chandrasekhar*, 1961], such as the boundary between the shocked SW (the magnetosheath) and the relatively stagnant magnetosphere [*Miura and Pritchett*, 1982]. Long established as a source for momentum and energy transport from the SW to the magnetosphere [*Miura*, 1984, 1987], later simulations and observations have shown non-linear stages of the KHI are also capable of reconnection and mass transport [*Nykyri and Otto*, 2001, 2004; *Nykyri et al.*, 2006; *Hasegawa et al.*, 2009] and ion heating via kinetic wave modes within the vortex [*Moore et al.*, 2016, 2017]. Compressional waves, like Kelvin-Helmholtz or ultra-low frequency (ULF) waves, can also lead to kinetic Alfvén wave (KAW) generation via mode conversion [*Johnson et al.*, 2001; *Chaston et al.*, 2007]. Recent work by *Nykyri et al.* [2021] has suggested that KAWs associated with the KHI can contribute to parallel electron heating, but in that case, were insufficient to account for the total heating. Identifying the detailed mechanism or mechanisms driving electron scale waves within the KHI and quantifying their contribution to electron heating is still an open question.

Observations have shown the KHI may form on both the dawn and dusk flanks under any orientation of the interplanetary magnetic field (IMF) [*Kavosi and Reader*, 2015], but simulations have shown a preference for dawn flank formation when the IMF is in a Parker Spiral (PS) orientation [*Nykyri*, 2013; *Adamson et al.*, 2016]. Work by *Henry et al.* [2017] analyzed the events presented in *Kavosi and Reader* [2015] and confirmed this preference observationally. *Henry et al.* [2017] also confirmed a preference for KHI formation at the dusk flank for high solar wind speeds under northward IMF (NIMF). As PS is the most statistically common IMF orientation, it follows that the associated preference for dawn-side KHI development would also be statistically more common. Such asymmetry in the formation of KHI, combined with KH-driven secondary processes like reconnection and kinetic scale waves, make the KHI a strong candidate to drive the dawn-dusk asymmetry of cold-component ions in the plasma sheet.

The launch of the Magnetospheric Multiscale (MMS) satellites presents a new opportunity to extend this study of the KHI and its associated secondary processes to smaller scales with higher resolution measurements. Within months of its launch, MMS had encountered KHI [*Eriksson et al.*, 2016]. The event reported by *Eriksson et al.* [2016] has been the subject of several case studies: *Li et al.* [2016] found evidence of Alfvénic ion jets and electron mixing due to reconnection at the trailing edge of the vortex; *Wilder et al.* [2016] noted compressed current sheets and evidence of ion-acoustic waves, and *Stawarz et al.* [2016] took advantage of MMS's high temporal and spatial resolutions to study turbulence generated by the KHI. These secondary processes would contribute to ion heating and plasma transfer across the magnetopause boundary.

Case studies are useful in identifying the fine-scale secondary processes associated with the KHI, but statistical studies are necessary to fully understand their role and quantify their contribution to heating and driving the plasma sheet asymmetry. It is therefore imperative, as a first step, to build a database of MMS encounters with KHI. Comparison of the location, duration, and prevailing IMF conditions of many events with the growth rates and unstable solid angles can help establish patterns which may prove informative in understanding the role KHI plays in magnetospheric dynamics (e.g., in generating dawn-dusk asymmetries via secondary,"cross-scale" processes or affecting the radiation belt electron populations via ULF wave generation or magnetopause shadowing).

In this paper we present a list of MMS encounters with the KHI and the physical characteristics of each, which may be used for future studies of small scale secondary processes. The MMS instrumentation and observational signatures used to identify the KHI encounters are described in Section 2.1 and 2.2, respectively. Growth rates and the unstable solid angle used to characterize the KHI are derived in Section 2.3 . Section 2.4 details the methodology used to separate magnetosheath and magnetospheric regions of the observed events, in order to caclulate the growth rates and unstable solid angle for each event. Results of these calculations are presented in Section 3. The methodology was also tested using 2-dimensional magnetohydrodynamic simulations as described in Section 4. Conclusions are presented and discussed in Section 5.

2 Methodology

2.1 MMS Instrumentation

Observational data reported here is level 2 survey data from MMS1 [*Burch et al.*, 2016]. Spacecraft separations are at most 230 km, and most often between 20 and 50 km, well below the typical size of the KHI, thus all spacecraft are expected to observe the same signatures and a single craft is sufficient to identify the KHI. Ion energy spectra and ion and electron moments are taken from the Fast Plasma Investigation (FPI) [*Pollock et al.*, 2016]. The Flux Gate Magnetometer (FGM) provides the DC magnetic field [*Russell et al.*, 2016; *Torbet et al.*, 2016]. Data file versions used are v3.3.0.cdf for FPI and v4.18.0.cdf for FGM. Solar wind data are taken from the OMNI database [*King and Papitashvili*, 2005].

2.2 Observational Signatures of the KHI

The KHI is known to occur at regions of large velocity shear, such as at the flank magnetopause. In this region the magnetosphere is relatively stagnant and plasma in the sheath is accelerating from low speeds immediately after the shock to "catch up" with the solar wind speed downtail [*Dimmock and Nykyri*, 2013]. At this boundary MMS observes a rapid change in ion bulk velocity on the order of several 100's of km/s. This change in bulk velocity, however, is characteristic of most boundary crossings even if the boundary is stable. A boundary perturbed by the KHI, which MMS may cross several times, exhibits quasi-periodic fluctuations in ion energies between typical magnetosheath and magnetospheric values. Similarly, anti-correlated, quasi-periodic signatures are also observed in the ion temperature and density for the unstable boundary. To distinguish the KHI from a shifting boundary (as a response to SW dynamic pressure variations) or other boundary instabilities (such as flux transfer events (FTE)), MMS is expected to observe quasi-periodic magnetic field fluctuations, particularly in the component of the field normal to the boundary, which indicate twisting of the field lines within the KH vortex. Total field strength will also vary due to compressions by the KHI. Additionally, the rotational nature of the KHI creates an outward force which is balanced by a pressure gradient, resulting in a decrease of total pressure at the center of the vortex. KHI events thus show a lower total pressure near the center of the vortex (where $\mathbf{B_N}$ is zero) and higher pressure in the spine region. This signature allows us to distinguish the KHI from a FTE in which total pressure typically increases when $\mathbf{B_N}$ is zero [*Nykyri et al.*, 2006; *Zhao et al.*, 2016].

Observed data is rotated into boundary normal (LMN) coordinates using the maximum variance of the electric field (MVA-E) technique. The general method for variance analysis techniques is given in *Sonnerup and Scheible* [1998]. *Nykyri et al.* [2011a,b] showed the single spacecraft MVA-E technique is sufficient for identification of the boundary normal direction when the plasma bulk velocity and magnetic field are primarily tangential to the boundary, as is typically in the case during KHI. It is also used here, rather than a multi-spacecraft method, to allow for automation of the analysis. For MVA-E, the direction in which the convective ($\mathbf{v}\times\mathbf{B}$) electric field variance is maximized (i.e., the direction of the maximum eigenvector of the variance matrix) is taken as the normal direction, $\mathbf{N}$. The 180° ambiguity in the normal direction is resolved by requiring the unit normal be positive pointing outward from the magnetosphere. Tangential directions, $\mathbf{L}$ and $\mathbf{M}$, are defined by the intermediate and minimum eigenvectors of the MVA-E matrix, but are not shown.

Figure 1 shows MMS1 survey level observations from 06:00 to 07:00 UT on 15 October 2015, the availability of burst mode for portions of the interval is indicated with a blue bar at the top of the figure. MMS passed through the dusk flank of the dayside mangnetopause during strongly dawnward IMF. The omni-directional ion energy spectrogram in panel (a) shows the expected quasi-periodic variations throughout the interval, which are well matched by anti-correlated changes in ion density and temperature (b). A velocity shear on the order of 200 km/s is visible near 06:26 UT in panel (c). The GSM magnetic field in panel (d) shows 20-40nT fluctuations characteristic of the KHI from 06:26 to 06:39 UT and again near from 06:48 to 06:55 UT. These fluctuations are also present in the normal component of the magnetic field (e). Decreases in total pressure (f) are visible starting around 06:27 UT and continuing through 06:48 UT. The decreases of total pressure correspond with times at which the normal magnetic field component is near 0, which is more clearly seen in Figure 2 from 06:37-06:38 UT.

Survey mode MMS1 observations of another KHI encounter on 26 September 2016 are shown in Figure 3 for the 70 minutes from 14:15 to 15:25 UT. The blue bar again indicates burst mode data is available for portions of the interval. MMS crossed the dusk flank magnetopause while the IMF was in a PS orientation. Quasi-periodic fluctuations in omni directional ion spectra are observable from approximately 14:20 to 15:20 UT in panel (a) and are accompanied by anti-correlated variations in ion density and temperature (b). Velocity shears (c) on the order of 150-200 km/s occur several times at approximately 14:30, 15:05, and again at 15:20 UT. Panel (d) shows fluctuations around 20 nT and up to 40 nT in the GSM magnetic field, which are also visible as 20-40nT changes in the normal component of the magnetic field (e). Decreases in total pressure are small, but observable in panel (f) from 14:35 to 15:10 UT. The normal component of the magnetic field is rarely near 0, making it difficult to correspond the small pressure decreases with the center of the vortex. This suggests MMS may have only skimmed the edge of the KHI, rather than crossing the vortex.

Table 1 summarizes the 50 MMS encounters with the KHI. MMS observed more KH events on the on the dusk side magnetopause (31) than on the dawn-side (19). Events are evenly distributed between the dayside and tail magnetopause: 25 events occur on either side of the terminator. Tail KHI are all observed in May 2017 and later, which is primarily due to a sampling effect of the MMS orbit change from Phase One which targeted the dayside magnetopause, to Phase Two which targeted the tail. The observed events ranged in duration from as little as 10 minutes to nearly 13 hours. Burst mode data is available for portions of all 50 events, which will be useful for future studies of smaller scale processes within the KHI.

Solar wind data from OMNI is available for 49 of the 50 events, which occur under a variety of IMF orientations and solar wind conditions. We consider the planar and B_Z components separately. At the time of event onset, the planar components of the IMF show a small preference for Parker Spiral (18) orientation followed closely by radial orientation (14). Less common are duskward (9), dawnward (6) and ortho-Parker Spiral (OPS) (2) orientations. For the duration of each event, the planar components of the average IMF configurations show a preference for the Parker spiral orientation (18), fol-

Table 1. The date, onset time, duration, GSM location, wavelength of 50 KHI events observed by MMS from September 2015 to March 2020. Burst mode data is available for portions of all events.

Date	Onset Time [UT]	Duration [min]	GSM Location [R_E]	KHI Wave-length [R_E]	Date	Onset Time [UT]	Duration [min]	GSM Location [R_E]	KHI Wave-length [R_E]
08 Sep 2015	09:00	170	[5.0, 7.4, -4.5]	2.80	20 May 2017	00:00	105	[-17.8, -16.6, -2.1]	20.76
15 Sep 2015	07:30	540	[5.2, 8.1, -4.9]	6.41	20 May 2017	02:00	150	[-17.6, -17.4, -0.6]	26.65
11 Oct 2015	10:30	30	[8.7, 6.5, -4.7]	3.71	28 May 2017	22:00	600	[-16.3, -16.6, 1.2]	9.13
15 Oct 2015	06:00	60	[9.0, 4.1, -2.3]	2.30	20 Sep 2017	22:32	43	[-10.8, 20.9, 1.3]	8.20
17 Oct 2015	16:00	28	[6.4, 7.8, -4.1]	4.94	26 Sep 2017	16:35	155	[-9.3, 19.6, -0.9]	6.47
18 Oct 2015	15:00	25	[7.2, 7.5, -4.4]	8.18	16 Oct 2017	14:30	50	[-4.0, 18.6, -2.7]	7.71
22 Dec 2015	22:15	35	[7.9, -5.7, -1.8]	2.58	30 Oct 2017	19:05	35	[-0.6, 17.3, 1.6]	4.20
11 Jan 2016	20:52	18	[6.2, -7.6, -3.4]	2.00	02 Nov 2017	17:25	50	[-0.9, 14.8, 0.8]	6.38
19 Jan 2016	19:55	40	[5.3, -8.2, -3.9]	3.24	04 Feb 2018	08:40	30	[8.8, -9.5, 1.4]	0.29
05 Feb 2016	18:55	35	[3.3, -9.3, -5.0]	5.97	03 May 2018	00:15	35	[-9.3, -17.5, -2.3]	8.43
07 Feb 2016	03:45	55	[7.0, -6.9, -3.5]	4.20	28 May 2018	20:50	150	[-15.9, -18.9, 1.4]	8.88
18 Feb 2016	19:30	70	[2.5, -9.7, -6.3]	6.80	18 Sep 2018	15:50	25	[-14.1, 20.6, -1.0]	5.17
25 Feb 2016	18:55	70	[1.3, -9.9, -6.5]	2.26	24 Sep 2018	14:10	195	[-14.1, 20.3, -1.6]	19.35
26 Sep 2016	14:15	70	[2.7, 8.5, -5.4]	12.57	02 Oct 2018	23:45	35	[-10.8, 22.5, 2.1]	11.26
27 Sep 2016	19:50	20	[0.3, 11.5, -3.4]	2.62	04 Oct 2018	17:25	10	[-0.8, 16.1, -0.2]	2.50
04 Oct 2016	18:20	70	[1.8, 11.2, -3.6]	9.51	13 Apr 2019	07:45	30	[-0.6, -17.5, 2.4]	9.68
10 Oct 2016	14:40	60	[4.3, 9.3, -5.0]	9.43	03 Jun 2019	23:05	75	[-2.2, -14.9, -3.8]	7.46
16 Oct 2016	20:20	10	[2.4, 11.1, -2.2]	8.83	25 Sep 2019	13:45	765	[-16.7, 22.0, -0.2]	12.33
24 Oct 2016	10:50	30	[6.8, 6.1, -4.3]	1.09	02 Oct 2019	08:15	165	[-9.9, 21.5, -4.5]	8.54
04 Nov 2016	11:45	75	[8.1, 7.2, -3.8]	2.28	02 Oct 2019	16:00	80	[-12.9, 23.5, -2.1]	13.03
22 Nov 2016	18:15	35	[6.6, 8.1, 0.2]	0.17	02 Oct 2019	21:40	25	[-14.6, 24.0, 1.1]	7.11
03 May 2017	02:00	150	[-12.9, -19.7, -3.9]	17.39	06 Oct 2019	14:50	175	[-14.8, 24.4, -4.2]	17.10
08 May 2017	13:00	110	[-14.8, -17.2, 0.3]	11.50	15 Oct 2019	19:00	75	[1.2, 12.8, 2.9]	8.81
11 May 2017	12:00	150	[-15.6, -18.2, 1.4]	18.47	22 Oct 2019	22:00	20	[1.8, 15.3, 3.8]	3.76
11 May 2017	15:44	31	[-15.3, -19.2, -0.3]	7.76	12 Nov 2019	20:30	75	[6.7, 11.8, 5.2]	7.04

lowed by radial and duskward (11 each) orientation. Dawnward (7) and OPS (2) orientations are less common. At event onset, the B_Z component of the IMF was more often northward (29) than southward (20). This preference for Northward IMF holds true for the duration of each event: 30(19) of the events occurred under average B_Z positive(negative).

Solar wind flow speeds are rarely less than 300 km/s or greater than 600 km/s. In the few cases when flow speed is outside the range, it is typically within a few km/s. One outlier occurs with solar wind flow speed over 700 km/s, but with very low solar wind density such that the Alfvén and fast mode speeds are large. The KHI is stabilized above the fast mode speed, but the large fast mode speed in this case allows the KH wave to develop [*Miura and Pritchett*, 1982]. The orientation of the magnetic field along the shear flow direction may also reduce the compressibility effects in this case. Solar wind parameters are discussed in more detail and correlated with KHI growth rates in Section 3. Values of the SW conditions for each event are available in the Supplement.

Having identified MMS encounters with the KHI, we next calculate the growth rates and unstable solid angles of the events and compare them with the prevailing solar wind and IMF properties.

2.3 Instability Growth Rate & Unstable Solid Angle

Any region unstable to the KHI will satisfy the KHI instability criteria

$$[\mathbf{k} \cdot (\mathbf{v_1} - \mathbf{v_2})]^2 \geq \frac{n_1 + n_2}{4\pi m_0 n_1 n_2} [(\mathbf{k} \cdot \mathbf{B_1})^2 + (\mathbf{k} \cdot \mathbf{B_2})^2] \tag{1}$$

where $\mathbf{v_i}$, n_i, and $\mathbf{B_i}$ are the the velocity, density, and magnetic field on either side of the velocity shear layer and $\mathbf{k}$ is the wave vector [*Chandrasekhar*, 1961].

Equation 1 may be rearranged to determine the normalized growth rate of the KHI in a particular region, which is defined as

$$Q/k = \sqrt{a_1 a_2 (\mathbf{\Delta v} \cdot \hat{\mathbf{k}})^2 - a_1 (\mathbf{v_{A1}} \cdot \hat{\mathbf{k}})^2 - a_2 (\mathbf{v_{A2}} \cdot \hat{\mathbf{k}})^2} \tag{2}$$

where a_i is a density parameter for either side of the boundary, defined by $a_i = \rho_i/(\rho_1 + \rho_2)$, $\mathbf{v_{Ai}}$ is the Alfvén velocity, and $\hat{\mathbf{k}}$ is the unit wave vector (thus the growth rate is normalized to the wavelength), pointing in the direction of maximum growth.

Note this equation is merely an approximation of the growth rate for an observed event as it assumes an infinitely thin boundary layer which is not true for the magnetopause. Equations 1 and 2 also assume an incompressible plasma, yet for high (> 600 km/s) solar wind speeds, the compressibility is generally sufficient to stabilize the development of the KHI. Due to these assumptions, the growth rate as determined by Equation 2 is an overestimate of the growth rate for an observed KHI. It must also be noted that MMS will not necessarily observe the source region of the KHI and local conditions may not match those of the source region. The difference in growth rate from the source region to the observation point is not predictable from observations.

In order to compare the growth rates for KHI events observed at various locations and under a variety of SW and IMF conditions, we make it completely unitless via normaliztion to the local fast mode speed, $v_{fm} = \sqrt{v_A^2 + c_s^2}$. Both magnetic tension and compressibility have stabilizing effects on the KHI. Likewise, the fast mode speed is dependent on the magnetic tension via the Alfvén velocity, v_A, and compressibility via the sound speed, c_s. Further, *Miura and Pritchett* [1982] showed the KHI growth rate is strongly correlated to the fast mode speed, and is stable for $Q/k > v_{fm}$, thus it is more physically meaningful to normalize to the fast mode speed than another characteristic speed.

The fast mode speed is not equal in the magnetosheath (sub-index msh) and magnetosphere (sub-index msp), so we normalize to the mean of the two, such that

$$Q_{unitless} = \frac{Q/k}{v_{fm}}$$

where $v_{fm} = \frac{1}{2}(v_{fmmsh} + v_{fmmsp})$.

In Equation 2 the direction of $\hat{\mathbf{k}}$ is chosen to maximize the normalized growth rate, but many directions of $\hat{\mathbf{k}}$ may satisfy the instability criteria. This range of angles capable of satisfying the instability criteria can be used to determine just how susceptible a region is to the development of the KHI.

The KHI may propagate in any direction $\hat{\mathbf{k}}$ for which Q/k is real (the right hand side of Equation 2 is positive under the square root). If we express $\hat{\mathbf{k}}$ in terms of the spherical angles ϕ and θ, the percent of the 4π solid angle that satisfies the KHI instability criteria at a given location may be calculated. We term this percentage the "unstable solid angle" [*Burkholder et al.*, 2020; *Nykyri et al.*, 2021]. Events with larger unstable solid angles are likely to be KHI, while cases with small growth rates can be indicative of a source region further upstream, such that the KHI has already created a more diffuse boundary layer.

2.4 Automated Region Sorting

Calculation of the growth rate and unstable solid angle requires the identification of separate regions of magnetosheath and magnetospheric plasma on either side of the magnetopause boundary. This is made difficult by the plasma mixing inherent within KH waves. In case studies it is common to select a few minutes of data in the pure magnetosheath and magnetosphere regions well away from the unstable boundary area. This is not, however, the most robust or efficient way to handle region identification for the many cases necessary for a statistical study. Instead, we seek to automate the process of separating the magnetosheath and magnetosphere regions.

The unperturbed flank magnetosheath is characterized by cold, dense plasma flowing tailward at high speeds with the shocked SW. In contrast the magnetospheric plasma near the flanks is hot, tenuous, and relatively stagnant. Thus, a combination of density, temperature, and the X-component of the bulk velocity may be used to separate data from the magnetosheath and magnetosphere regions. The isolated data then provides the mean values of density, velocity, etc. used in the calculation of the growth rates and unstable solid angle.

The magnetosheath is identified by the product of ion density and tailward velocity divided by the average ion temperature, nv_{tail}/T. The GSM X velocity component, v_X, is measured to be large and negative in the sheath and small, either positive or negative, in the magnetosphere. To simplify our parameter, we shift the tailward velocity to be strictly positive with a minimum value at 0, such that $v_{tail} = |v_X - \max(v_X)|$. The resulting parameter, nv_{tail}/T, is thus large in the magnetosheath and small in the magnetosphere. We identify the sheath as any region in which the value of nv_{tail}/T is greater than 1.5 times the magnetopause value. The magnetopause value is defined as the mean of the largest 12.5% and smallest 12.5% of all nv_{tail}/T values (for a total of 25% of available data) for each event. This method allows us to reliably identify the magnetosheath regions near the KHI while avoiding the inclusion of mixed and transition regions in our calculations of the KHI growth rate and unstable solid angle (see the Supplementary Information for details justifying the data ranges and cutoff values presented here).

The nv_{tail}/T parameter does not, however, reliably isolate magnetospheric plasma. Instead, we use the ion specific entropy, $S = T/n^{2/3}$, to identify magnetospheric regions within each KHI event. The hot, tenuous magnetosphere has much higher specific entropy than the magnetosheath, so we may follow the same procedure as employed for isolating the magnetosheath with specific entropy in place of the nv_{tail}/T parameter to separate the magnetosphere. That is, any region with specific entropy 1.5 times greater than the magnetopause value is considered to be the magnetosphere. Again the magnetopause value is the mean of the largest 12.5% and smallest 12.5% (25% total) of all entropy values for the event. This allows for reliable determination of the magnetospheric regions near the KHI without including mixed and transition plasma regions (see Supplementary Information).

Figures 4 and 5 depict time series of both parameters, nv_{tail}/T (a), and S (b) for the example events. Solid lines show the magnetopause value of each parameter, and dashed lines indicate the cutoff value at 1.5 time the magnetopause value. Colored boxes highlight the regions identified as the magnetosheath (blue) and magnetosphere (red). In both example events, the identified regions match well with those parts of the omnidirectional ion spectrogram (c) and density and temperature time series (d) which correspond to typical magnetosheath and magnetospheric values.

Having isolated the separate regions, we then calculate mean values of density, temperature, velocity, and magnetic field on either side of the boundary. These values are checked to ensure they fall within typical ranges for the magnetosheath and magnetosphere before they are used in calculation of the growth rate and unstable solid angle. The new method was also tested using simulation data, and provided good agreement with the known values (see Section 4).

Growth rate alone is not a sufficient parameter to describe the KHI. The KHI is a convective instability which dissipates stored energy as it develops, thus growth rate and the unstable solid angle are maximized just prior to the formation of the KH vortex. The nature of in-situ observations, however, dictates we cannot identify a KHI until it is relatively well developed. Thus small growth rates and unstable solid angles are not necessarily counter-indicative of the presence of the KHI, but may instead be features of later stage KH waves.

As a secondary check for events with low growth rates, we plot tailward velocity as a function of density to see if the KHI vortex had rolled over, examples of which are seen in Figures 6 and 7. As the KHI develops, it may form non-linear vortices in which low density magnetospheric plasma becomes trapped and is drug tailward with magnetosheath-like velocities. This is seen in observations as low density magnetospheric plasma flowing tailward with the magnetosheath [*Hasegawa et al.*, 2006; *Taylor et al.*, 2012], and is apparent as points in the lower left quadrant of Figures 6 and 7. For the 15 October 2015 event, only the electrons, due to their smaller mass and inertial length, show signatures of roll-over. For the 26 September 2016 event, both ions and electrons indicate the KHI has rolled over to form a vortex. In both cases, the rolled-over plasma is considered mixed or ambiguous, despite having density more characteristic of the magnetosphere. This is a good indicator that our method of automatically separating regions is selecting only pure magnetosheath and magnetospheric plasmas and excluding regions where the KHI has already caused mixing.

Another indicator of vortex roll-over within the KHI is a comparison of the normal component with the total bulk velocity. At a quiet boundary, plasma bulk velocity is generally tangential to the boundary. As a KHI twists the boundary, the normal component of the velocity increases. For a well developed vortex, the maximum value of the normal velocity will be a significant fraction of the total velocity.

3 Observational Results

Having separated the magnetosheath and magnetospheric regions of each event, growth rates, unitless growth rates, and unstable solid angles are calculated. Results for all 50 events are listed in Table 2. Growth rates range from 0.16 to 103.16 km/s. When normalized to the fast mode speed, unitless growth rates range from 0 to 0.325, but more typically are between 0.010 and 0.200. That is the KHI typically develops at 1-20% of the local fast mode speed; only 3 events fall below this range and 7 above it. Unstable solid angles range from 0.0 to 39.51. At its maximum, the normal component of velocity often accounts for more than 60%, and occasionally all, of the total velocity, indicating the observed KH waves have significantly twisted the boundary. Events with strongly twisted boundaries are good candidates for future studies of reconnection and other secondary processes driven by the KHI.

Growth rates (GR), unitless growth rates (UGR), and unstable solid angles show some dependence on location, as can be seen in Figure 8. The locations of the KHI events observed by MMS are plotted in the GSM X-Y (left column), X-Z (middle column), and

Table 2. Growth Rates (GR), unitless GR, and unstable solid angles (SA) for each of the 50 KHI events observed by MMS from September 2015 to March 2020. At its maximum, the normal velocity component is a significant fraction of the total velocity for most events.

Event Date	GR [km/s]	Unitless GR	Unstable SA [%]	v_{Nmax} $/v_{tot}$	Event Date	GR [km/s]	Unitless GR	Unstable SA [%]	v_{Nmax} $/v_{tot}$
08 Sep 2015	81.63	0.081	6.37	0.96	20 May 2017	88.49	0.181	28.44	0.93
15 Sep 2015	19.63	0.023	1.52	0.99	20 May 2017	47.42	0.066	30.22	0.76
11 Oct 2015	15.68	0.016	0.42	0.58	28 May 2017	70.68	0.168	16.79	0.93
15 Oct 2015	8.83	0.007	0.11	0.86	20 Sep 2017	53.99	0.145	18.75	0.19
17 Oct 2015	25.05	0.032	4.01	0.93	26 Sep 2017	52.31	0.189	24.28	0.82
18 Oct 2015	52.41	0.063	9.07	0.96	16 Oct 2017	26.03	0.047	6.74	0.79
22 Dec 2015	10.41	0.010	0.29	0.83	30 Oct 2017	11.51	0.023	4.70	0.97
11 Jan 2016	17.47	0.015	0.27	0.89	02 Nov 2017	39.55	0.109	5.95	0.66
19 Jan 2016	13.69	0.024	0.12	0.52	04 Feb 2018	14.74	0.085	38.95	0.62
05 Feb 2016	22.31	0.028	5.74	0.93	03 May 2018	95.59	0.325	23.37	0.97
07 Feb 2016	13.36	0.019	0.16	0.66	28 May 2018	15.79	0.062	3.21	0.31
18 Feb 2016	34.90	0.038	8.96	1.00	18 Sep 2018	40.97	0.090	9.96	0.90
25 Feb 2016	5.00	0.012	0.08	0.68	24 Sep 2018	71.15	0.227	36.91	0.73
26 Sep 2016	51.46	0.068	7.26	0.99	02 Oct 2018	41.17	0.111	10.18	0.65
27 Sep 2016	84.07	0.117	8.37	0.96	04 Oct 2018	31.26	0.081	6.16	0.50
04 Oct 2016	54.67	0.062	7.17	0.70	13 Apr 2019	48.93	0.089	15.66	0.76
10 Oct 2016	43.30	0.059	8.98	0.75	03 Jun 2019	42.25	0.108	16.63	0.94
16 Oct 2016	65.56	0.070	7.35	0.57	25 Sep 2019	74.22	0.198	28.04	0.84
24 Oct 2016	3.93	0.005	0.06	0.71	02 Oct 2019	29.28	0.083	6.10	0.59
04 Nov 2016	16.78	0.019	0.78	0.94	02 Oct 2019	96.46	0.209	26.71	0.81
22 Nov 2016	0.16	0.000	0.00	0.87	02 Oct 2019	37.12	0.111	18.09	0.52
03 May 2017	56.65	0.197	39.51	0.85	06 Oct 2019	82.42	0.210	34.49	0.98
08 May 2017	84.15	0.278	29.87	1.00	15 Oct 2019	94.08	0.296	18.37	0.98
11 May 2017	45.56	0.103	12.07	0.88	22 Oct 2019	52.52	0.110	12.00	1.00
11 May 2017	49.99	0.198	13.33	0.34	12 Nov 2019	103.16	0.250	14.34	0.90

Y-Z (right column) planes and color coded according to the growth rate (top row), unitless growth rate (middle row), and unstable solid angle (bottom row). KHI observed near the sub-solar point tend to have lower growth rates than those observed further along the magnetopause, particularly those observed along the tail. This is still apparent even when growth rates are normalized to the local fast mode speeds. This is likely due to the low velocity shear near the subsolar point. Immediately after the bow shock, the magnetosheath plasma is slowed signficantly from solar wind speeds, and the shear between the sheath and magnetosphere is much lower than further downtail, where the magnetosheath plasma has accelerated and returned to solar wind velocity. The low velocity shear near the subsolar point will result in lower growth rates, as can be seen from Equation 2.

Unstable solid angles show a similar pattern as the growth rates, with larger values observed further down tail. Again, this can be explained by the large velocity shears encountered along the tail magnetopause. On the dayside, the shocked solar wind of the magnetosheath is still accelerating back up to solar wind speed after encountering the obstacle of earth's magnetosphere and bow shock, thus velocity shears between the sheath and magnetosphere are smaller. Further down tail, the magnetosheath plasma has reachieved the high solar wind flow speed, thus increasing the shear between the two regions. For larger velocity shears the stabilizing effects of the magnetic field are less influential in the development of KHI, and a larger solid angle is thus unstable to the growth of the KHI.

A cluster of KHI events occur at high southern magnetic latitudes (GSM-Z $< -4.5R_E$), showing the KHI is not limited to lower latitudes. This is a new finding, as previous missions, such as THEMIS, remained at lower magnetic latitudes. Only three prior studies, two using Cluster data [*Hwang et al.*, 2012; *Ma et al.*, 2016], and one using MMS data [*Nykyri et al.*, 2021], have been conducted on the KHI at high latitudes near the dawn and dusk flanks of the high-altitude cusps.

Figures 9, 10, and 11 plot the growth rate, unitless growth rate, and unstable solid angle, respectively, of 49 of the 50 events as a function of solar wind density (a), temperature (b), flow speed (c), Alfvén Mach number (d), pressure (e), and IMF magnitude (f) taken from OMNI data. OMNI data was not available for one event. Colors within the plots correspond with event dates and times, so each event is shown with the same color in all plots for direct comparison.

Solar wind density ranges from 2.6 to 17.0 /cc. Observed events are well distributed over the density range, and no relationship is apparent between density and growth rates or unstable solid angles. Temperatures generally range from 0.7 to 31.4 eV, with one outlier event occurring with a solar wind temperature of 61.0 eV. Most events are observed for solar wind temperatures less than 20 eV, but no trend in growth rate or unstable solid angle is apparent.

There is an apparent selection window in the solar wind flow speed, with all but one event occurring when solar wind flow is between 295 and 610 km/s. This fits with expectations that low velocity shears between the sheath and magnetosphere are not unstable to the KHI, and compressibility effects for very large shears stabilize the KHI [*Miura and Pritchett*, 1982]. One outlier event occurs during a period of solar wind flow speed ≈ 710 km/s. The SW density in this case is very small and the Alfvén Mach number is ≈ 11, similar to many other events. The lower density and Mach number indicate a large Alfvén speed, and correspondingly large fast mode speed. As the KHI is stabilized above the fast mode speed, the large fast mode speed allows for the KHI to develop even for the very large SW flow speed in this case.

Alfvén Mach numbers also show no clear relationship to growth rate or unstable solid angle. Events are observed for Alfvén Mach numbers between 3.8 and 26.3, though most events occur when the Mach Number is below 20.

IMF magnitude for all but one event is greater than 1.5 nT and less than 11.2 nT. The outlier event occurred for an average IMF magnitude of 20.8 nT. Events are otherwise evenly distributed throughout the range of IMF magnitudes with no apparent relationship to growth rate or unstable solid angle.

Other than the selection window for solar wind flow speed, growth rate, unitless growth rate, and unstable solid angle are not correlated with solar wind conditions.

The solar wind conditions and IMF orientations, however do help explain the observation of more KHI on the dusk side of the magnetopause than on the dawn side. *Henry et al.* [2017] found dusk flank formation to be more common both for high solar wind speeds (> 400 km/s) and Northward IMF orientations. 27 of the 50 events occur when solar wind speeds were high, and 30 of the 50 events had IMF orientations with positive B_Z components.

4 Comparison with Simulations

To verify our method of isolating regions on either side of the boundary is robust, it was applied to parameters generated by two dimensional MHD simulations of the KHI. A simulation case for a KHI developing under Northward IMF (NIMF) conditions was tested using initial conditions comparable to those of the event on 08 September 2015. A second simulation case used initial conditions similar to those of the 18 October 2015 event for the KHI developing on the dusk flank under Parker Spiral IMF (PSIMF) orientation.

The simulations, after *Ma et al.* [2019], solve the full set of resistive Hall-MHD equations equations using a leapfrog scheme [*Potter*, 1973; *Birn*, 1980; *Otto*, 1990]. We normalize all physical quantities to their typical scale, for example, the length L is normalized to L_0, the half width of the initial sheared flow; number density to n_0, the magnetic field to B_0, velocity to the Alfvén velocity, $v_A = B/\sqrt{\mu_0 \rho_0}$; and the time to the Alfvén transit time $T_A = L_0/v_A$. Exact values of the the normalizations for both simulation cases are listed in the Supplement.

A cut is taken through the simulation box at every time step. Data from these cuts are separated into distinct regions using the method described in Section 2.4, then used to calculate growth rates and unstable solid angles. The growth rate as a function of time is shown in black in panel (a) of Figures 12 and 13 for the NIMF and PSIMF cases respectively. The growth rate of the observation case on which the simulations are based is also shown in magneta, and the simulation growth rate, as determined by the linear slope of a plot of $\ln(v_\perp)$ as a function of time, is shown in green. Examples of the density at various time steps show the development of the KHI (panels b-f). The cuts used for calculations are shown in red in the same panels.

As can be seen in Figures 12 and 13, the KHI growth rate increased from its initial value until the cut through the simulation captured vortex roll-over. After roll-over is observed, growth rate decreases sharply then increases towards its initial level as the instability dissipates. All of this is consistent with expectations: the free energy available to drive the KHI peaks before the vortex forms. The KHI then dissipates the energy.

In both cases, growth rates calculated using Equation 2 are significantly greater than the simulation growth rate. This is to be expected as Equation 2 assumes an infinitely thin boundary layer and incompressible plasma; the simulation growth rate is free from these assumptions.

Within the first few time steps, the simulation matches well with the observed growth rate for the NIMF case. The growth rate of the event the NIMF simulation is based on is 81.63 km/s. The initial growth rate for the simulation is 82.74 km/s, and remains within 5 km/s of the observed growth rate for more than 80 time steps. That is, the first 20% of the simulation is in rough agreement with the observation.

The PSIMF simulation shows poorer agreement with the observed event on which it is based. The observed event has a growth rate of 52.41 km/s, but the initial simulation value is 72.68 km/s. This may be due to a few factors. First, We note the growth rate is dependent upon the geometry of the cut through the KH wave. The method of separating the two regions works best when a the spacecraft spends a significant portion of the event duration on both sides of the boundary. It is more difficult to separate the regions for events in which the spacecraft merely skims the vortex or spends significantly more time in one region than the other, and such events may actually grow faster than our calculations would indicate. The cut we take through the simulation represents an ideal encounter in which the spacecraft spends nearly equal time on either side of the boundary and passes directly through the vortex center. Such an ideal path is unlikely for observational data. Second, the observation case on which the PSIMF simulation is based occurred at relatively high magnetic latitude (GSM$-Z = -4.4R_E$) and the local MHD simulations may not capture a high-latitude onset region.

5 Conclusions and Discussion

The main conclusions may be summarized as follows:

- MMS observed 50 clear KHI events from September 2015 to March 2020.

From September 2015 to March 2020 MMS observed more than 100 unique mixed regions which initially resembled the KHI. Further analysis of total pressure and boundary-normal rotated magnetic field showed 50 of these events likely to be the KHI. These 50 events, summarized in Table 1, occur under a variety of prevailing SW conditions and IMF orientations.

These 50 events form the beginnings of a database for statistical studies of the KHI and its associated secondary processes. Burst mode data is available for portions of all the identified events. This is useful and necessary for future studies of secondary processes approaching the electron scale. The methods developed here may also be applied to the MMS data from April 2020 to present to further extend the database of events for analysis.

- An automated method uses nv_{tail}/T and specific entropy to identify the magnetosheath and magnetospheric regions, respectively, within a KH wave event. This method consistently isolates the pure regions, and excludes mixed plasma, both for real satellite and simulated data.

The identified magnetosheath and magnetospheric regions of each KHI event match well with the omni-directional ion energy spectrogram and density and temperature time series. Mean values of density, temperature, velocity, and magnetic field in the identified regions are consistent with typical values. Plots of the GSM $X-$velocity and density show mixed regions are successfully avoided. See the Supplementary Information for more details on the development of the presented method and rejected alternatives.

In simulations the density within the identified regions throughout the simulation is within 0.15/cc of the initial value for the NIMF case and 0.3/cc of the initial value for the PSIMF case. Thus our method of isolating the pure magnetosheath and magnetosphere is reliable and robust even for late stage KHI with roll-over and mixing.

When comparing the results of the simulation and the observation, we see good agreement for the growth rate for the NIMF case. The PSIMF case showed poorer agreement, but this is likely due to the geometry of the cut through the simulation and the path of MMS through the observed event. The particular event on which the PSIMF simulation is based also occurred at a relatively high southern latitude (GSM$-Z = -4.4R_E$). The local MHD simulations would not capture a high-latitude onset region.

- Plasma parameters from the automatically isolated regions were used to calculate KHI growth rates, unitless growth rates, and unstable solid angles for the 50 KHI events in our database.

Growth rates, unitless growth rates normalized to the local fast mode speed, and unstable solid angles for the 50 KHI events in our database are reported in Table 2.

Growth rates range from a minimum of 0.16 to 103.16 km/s. When normalized to the fast mode speed, the unitless growth rate ranges from 0.000 to 0.325 in the extremes, with most events in the 0.01 to 0.20 range. That is, most of the observed KHI grow at a speed that is between 1% and 20% of the local fast mode speed.

Ten of the events have unstable solid angles less than 1% of the total 4π solid angle. Unstable solid angles are between 1% and 10% for 8 events, and between 10% and 25% for 13 events. 9 events have unstable solid angles greater than 25% of the total 4π solid angle. Larger solid angles are more common further down tail where the velocity shear from the magnetosheath to the magnetosphere is greater and thus the stabilizing effects of the magnetic field are less influential.

We note several of the observed events occur in apparently stable regions with very low growth rates; this does not preclude the observed events from being the KHI. Convective instabilities, like the KHI, dissipate energy stored in unstable regions and systems. As excess energy is dissipated, the region becomes more stable, thus maximum instability and growth rates occur just prior to the formation of the instability. The KHI, by necessity, is only observed after instability and growth rates have decreased from their maxima. We believe those events occurring in apparently more stable regions may be later in development than faster growing KHI in less stable areas.

We also note the path MMS takes through the KHI event can have a significant effect on the growth rate determination. Encounters which merely skim the KH vortex rather than passing directly through it may actually grow faster than our calculations would indicate.

- The KHI is typically observed when solar wind flow speeds are between 295 and 610 km/s. Within this flow speed selection window, KHI growth rates and unstable solid angles are independent of prevailing solar wind conditions.

Values of the growth rate, unitless growth rate, and unstable solid angle for each event are listed in Table 2. As can be seen in Figures 9, 10, and 11, growth rate, unitless growth rate, and unstable solid angle appear to be independent of solar wind conditions, with the exception of solar wind flow speed. All but one of the observed events occurred when the solar wind speed was between 295 and 610 km/s. At flow speeds much below 295 km/s the velocity shear is too low to satisfy the KHI onset conditions (Equation 1). At solar wind speeds above 610 km/s the compressibility of the plasma will usually stabilize the KHI [*Miura and Pritchett*, 1982]. Only one event occurred with flow speed significantly greater than 610 km/s, but given the low solar wind density and Alfvén Mach number during that event, compressibility effects were probably small. Within this selection window between 295 and 610 km/s however, flow speed is not correlated with growth rate, unitless growth rate, or unstable solid angle.

The database of MMS KHI observations presented here will be used in future studies of secondary processes associated with the KHI. The availability of burst mode data for all 50 events allows studies of secondary KHI processes to be extended to smaller spatial and temporal scales. The trends we have observed in the location and SW and IMF conditions may also be used to simplify the search for and identification of future KHI events.

Acknowledgments

Funding for this work was provided by the National Science Foundation under grant number 1707521 and by NASA under grants numbers NNZ17AI50G and NNX16AF89G. Thanks are owed to the entire MMS team, and especially to the FGM and FPI instrument groups. MMS data was retrieved from the MMS Science Data Center at lasp.Colorado.edu/mms/sdc/public. OMNI solar wind data is available from NASA Goddard Space Flight Center's Space Physics Data Facility at omniweb.gsfc.nasa.gov.

References

Adamson, E., K. Nykyri, and A. Otto (2016), The Kelvin-Helmholtz instability under Parker-spiral interplanetary magnetic field conditions at the magnetospheric flanks, *Advances in Space Research*, *58*.

Axford, W., and C. Hines (1961), A unifying theory of high-Latitude phenomena and geomagnetic storms, *Canadian Journal of Physics*, *39*, 1433–1464.

Birn, J. (1980), Computer studies of the dynamic evolution of the geomagnetic tail, *Journal of Geophysical Research*, *85*, 1214–1222.

Burch, J. L., and T. D. Phan (2016), Magnetic reconnection and the dayside magnetopause: advances with MMS, *Geophysical Research Letters*, *43*, 8327–8338, doi:10.1002/2016GL069787.

Burch, J. L., T. E. Moore, R. B. Torbet, and B. L. Giles (2016), Magnetospheric Multiscale overview and science objectives, *Space Science Reviews*, *199*, 5–21, doi:10.1007/s11214-015-0164-9.

Burkholder, B. L., K. Nykyri, X. Ma, R. Rice, S. A. Fuselier, K. J. Trattner, K. R. Pritchard, J. L. Burch, and S. M. Petrinec (2020), Magnetospheric multiscale observation of an electron diffusion region at high latitudes, *Geophysical Research Letters*, *47*(15), doi:10.1029/2020GL087268.

Chandrasekhar, S. (1961), *Hydrodynamic and Hydromagnetic Stability*, Oxford University Press.

Chaston, C. C., M. Wilber, M. Fujimoto, M. L. Goldstein, M. Acuna, H. Rme, and A. Fazakerley (2007), Mode conversion of anomalous transport in Kelvin-Helmholtz vortices and kinetic Alfvn waves at Earth's magnetopause, *Physical Review Letters*, *99*.

Dimmock, A. P., and K. Nykyri (2013), The statistical mapping of magnetosheath plasma properties based on THEMIS measurements in the magnetosheath enterplanetary medium reference frame, *Journal of Geophysical Research*, *118*, 4963–4876.

Dimmock, A. P., K. Nykyri, H. Karimbadi, A. Osmane, and T. I. Pulkkinen (2015), A statistical study into the spatial distribution and dawn-dusk asymmetry of dayside mangetosheath ion temperatures as a function of upstream solar wind conditions, *Journal of Geophysical Research*, *120*, 2767–2782, doi: 10.1002/2014JA020734.

Eriksson, S., B. Lavraud, F. D. Wilder, J. E. Stawarz, B. L. Giles, J. L. Burch, W. Baumjohann, R. E. Ergun, P.-A. Lindqvist, W. Magnes, C. J. Pollock, C. R. Russel, Y. Saito, R. J. Strangeway, R. B. Torbert, D. J. Gershmann, Y. V. Khotyaintsev, J. C. Dorelli, S. J. Schwartz, L. Avanov, E. Grimes, Y. Vernisses, A. P. Sturner, T. D. Phan, G. T. Marklund, T. E. Moore, W. R. Paterson, and K. A. Goodrich (2016), Magnetospheric multiscale observations of magnetic reconnection associated with Kelvin-Helmholtz waves, *Geophysical Research Letters*, *43*, 5606–5615, doi:10.1002/2016GL068783.

Fairfield, D. H., A. Otto, T. Mukai, S. Kokubun, R. P. Lepping, J. T. Steinberg, A. J. Lazaurs, and T. Yamamoto (2000), Geotail observations of the Kelvin-Helmholtz instability at the equatorial magnetotail boundary for parallel northward fields, *Journal of Geophysical Research*, *105*.

Foullon, C., C. J. Farrugia, A. N. Fazakerley, C. J. Owen, F. T. Gratton, and R. B. Torbert (2008), Evolution of Kelvin-Helmholtz activity on the dusk flank magnetopause, *Journal of Geophysical Research*, *113*, doi:10.1029/2008JA013175.

Gosling, J. T., M. F. Thomsen, S. J. Bame, and C. T. Russell (1986), Accelerated plasma flows at the near-tail magnetopause, *Journal of Geophysical Research: Space Physics*, *91*, doi:10.1029/JA091iA03p03029.

Hasegawa, H., M. Fujimoto, K. Maezawa, Y. Saito, and T. Mukai (2003), Geotail observation of the dayside outer boundary region: Interplanetary magnetic field control and dawn-dusk asymmetry, *Journal of Geophysical Research*, *108*, doi:10.1029/2002JA009667.

Hasegawa, H., M. Fujimoto, T.-D. Phan, H. Réme, A. Balogh, M. W. Dunlop, C. Hashimoto, and R. TanDokoro (2004), Transport of solar wind into Earth's magnetosphere through rolled-up Kelvin-Helmholtz vortices, *Nature*, *430*, 755–758.

Hasegawa, H., M. Fujimoto, K. Takagi, Y. Saito, T. Mukai, and H. Réme (2006), Single-spacecraft detection of rolled-up Kelvin-Helmholtz vortices at the flank magnetopause, *Journal of Geophysical Research*, *111*, doi:10.1029/2006JA011728.

Hasegawa, H., A. Reino, A. Vaivads, Y. Khotyaintsev, M. Andre, T. K. M. Nakamura, L.-L. Teh, B. U. O. Sonnerup, S. J. Schwartz, Y. Seki, M. Fujimoto, Y. Saito, H. Reme, and P. Canu (2009), Kelvin-Helmholtz waves at the Earth's magnetopause: multiscale development and associated reconnection, *Geophysical Research Letters*, *114*, doi:10.1029/2009JA014042.

Henry, Z. W., K. Nykyri, T. W. Moore, A. P. Dimmock, and X. Ma (2017), On the dawn-dusk asymmetry of the Kelvin-Helmholtz instability between 2007 and 2013, *Journal of Geophysical Research*, *122*, 11,888–11,900, doi:10.1002/2017JA024548.

Hwang, K.-J., M. L. Goldstein, M. M. Kuznetsova, Y. Wang, A. F. Vias, and D. G. Sibeck (2012), The first in situ observation of kelvin-helmholtz waves at high-latitude magnetopause during strongly dawnward interplanetary magnetic field conditions, *Journal of Geophysical Research: Space Physics*, *117*(A8), doi: 10.1029/2011JA017256.

Johnson, J. R., C. Z. Cheng, and P. Song (2001), Signatures of mode conversion and kinetic Alfvn waves at the magnetopause, *Geophysical Research Letters*, *28*.

Kavosi, S., and J. Reader (2015), Ubiquity of Kelvin-Helmholtz waves at the Earth's magnetopause, *Nature Communications*.

King, J. H., and N. E. Papitashvili (2005), Solar wind spatial scales in and comparisons of hourly wind and ACE plasma and magnetic field data, *Journal of Geophysical Research*, *110*, doi:10.1029/2004JA010649.

Li, W., M. Andre, Y. V. Khotyaintsev, A. Vaivads, D. B. Graham, S. Toledo-Redondo, C. Norgren, P. Henri, C. Wang, B. B. Tang, B. Lavraud, Y. Vernisse, D. L. Turner, J. Burch, R. Torbet, W. Magnes, C. T. Russell, J. B. Blake, B. Mauk, B. Giles, C. Pollock, J. Fennell, A. Jaynes, L. A. Avanov, J. C. Dorellie, D. J. Gershman, W. R. Paterson, Y. Saito, and R. J. Strangeway (2016), Kinetic evidence of magnetic reconnection due to Kelvin-Helmholtz waves, *Geophysical Research Letters*, *43*, 5635–5643, doi:10.1002/2016GL069192.

Lin, D., C. Wang, W. Li, B. Tang, X. Guo, and Z. Peng (2014), Properties of Kelvin-Helmholtz waves at the magnetopause under northward interplanetary magnetic field: statistical study, *Journal of Geophysical Research: Space Physics*, *119*, 7485–7494, doi:10.1002/2014JA020379.

Ma, X., A. Otto, and P. Delamere (2014a), Interaction of magnetic reconnection and Kelvin-Helmholtz modes for large magnetic shear: 1. Kelvin-Helmholtz trigger, *Journal of Geophysical Research: Space Physics*, *119*, 781–797, doi: 10.1002/2013JA019224.

Ma, X., A. Otto, and P. Delamere (2014b), Interation of magnetic reconnection and Kelvin-Helmholtz modes for large magnetic shear: 2. reconnection trigger, *Journal of Geophysical Research: Space Physics*, *119*, 808–820, doi:10.1002/2013JA019225.

Ma, X., A. Otto, P. A. Delamere, and H. Zhang (2016), Interaction between reconnection and kelvin–helmholtz at the high-latitude magnetopause, *Advances in Space Research*, *58*(2), 231–239.

Ma, X., P. Delamere, A. Otto, and B. Burkholder (2017), Plasma transport driven by the three-dimensional Kelvin-Helmholtz instability, *Journal of Geophysical Research: Space Physics*, *122*, 10,382–10,395, doi:10.1002/2017JA024394.

Ma, X., P. Delamere, K. Nykyri, B. Burkholder, D. Neupane, and R. Rice (2019), Comparison between fluid simulation with test particles and hybrid simulation for the Kelvin-Helmholtz instability, *Journal of Geophysical Research: Space Physics*, *124*, 6654–6668, doi:10.1029/2019JA026890.

Merkin, V. G., J. G. Lyon, and S. G. Claudepierre (2013), Kelvin-Helmholtz instability of the magnetospheric boundary in a three-dimensional global MHD simulation during northward IMF conditions, *Journal of Geophysical Research: Space Physics*, *118*, 5478–5496, doi:10.1002/jgra.50520.

Miura, A. (1984), Anomalous transport by magnetohydrodynamic Kelvin-Helmholtz instabilities in the solar wind-magnetosphere interaction, *Journal of Geophysical Research*, *89*, 801–818.

Miura, A. (1987), Simulation of the Kelvin-Helmholtz instability at the magnetospheric boundary, *Journal of Geophysical Research*, *92*, 3195–3206.

Miura, A., and P. L. Pritchett (1982), Nonlocal stability analysis of the MHD Kelvin-Helmholtz instability in a compressible plasma, *Journal of Geophysical Research*, *87*, 7431–7444.

Moore, T. W., K. Nykyri, and A. P. Dimmock (2016), Cross-scale energy transport in space plasmas, *Nature Physics*.

Moore, T. W., K. Nykyri, and A. P. Dimmock (2017), Ion-scale wave properties and enhanced ion heating across the low-latitude boundary layer during Kelvin-Helmholtz instability, *Journal of Geophysical Research: Space Physics*, *122*, 11,128–11,153, doi:10.1002/2017JA024591.

Nykyri, K. (2013), Impact of MHD shock physics on magnetosheath asymmetry and Kelvin-Helmholtz instability, *Journal of Geophysical Reseach: Space Physics*, *118*, 5068–5081.

Nykyri, K., and A. Otto (2001), Plasma transport at the magnetopause boundary due to reconnection in Kelvin-Helmholtz vortices, *Geophysical Research Letters*, *28*, 3565–3568.

Nykyri, K., and A. Otto (2004), Influence of the Hall term on KH instability and reconnection inside KH vortices, *Annales Geophysicae*, *22*, 935–949.

Nykyri, K., A. Otto, , J. Büchner, B. Nikutowski, W. Baumjohann, L. M. Kistler, and C. Mouikis (2003), Equator-S observations of boundary signatures: FTE's or Kelvin-Helmholtz waves?, in *Earth's Low-Latitude Boundary Layer*, *Geophys-*

ical Monograph, vol. 133, edited by P. T. Newell and R. Onsager, pp. 205–210, American Geophysical Union.

Nykyri, K., A. Otto, B. Lavraud, C. Mouikis, L. M. Kistler, A. Balogh, and H. Réme (2006), Cluster observations of reconnection due to the Kelvin-Helmholtz instability at the dawnside magnetospheric flank, *Annales Geophysicae*, *24*, 2619–2643.

Nykyri, K., A. Otto, E. Adamson, and J. Mumme (2011a), Cluster observations of a cusp diamagnetic cavity: structure, size, and dynamics, *Journal of Geophysical Research*, *116*, doi:10.1029/2010JA015897.

Nykyri, K., A. Otto, E. Adamson, and A. Tjulin (2011b), On the origin of fluctuation in the cusp diamagnetic cavity, *Journal of Geophysical Research*, *116*, doi:10.1029/2010JA015888.

Nykyri, K., X. Ma, A. Dimmock, C. Foullon, A. Otto, and A. Osmane (2017), Influence of velocity fluctuations on the Kelvin-Helmholtz instability and its associated mass transport, *Journal of Geophysical Research*, *122*, 9489–9512, doi: 10.1002/2017JA024374.

Nykyri, K., X. Ma, B. Burkholder, R. Rice, J. R. Johnson, E.-K. Kim, P. Delamere, A. Michael, K. Sorathia, D. Lin, S. Merkin, S. Fuselier, J. Broll, O. Le Contel, D. Gershman, I. Cohen, B. Giles, R. J. Strangeway, C. T. Russell, and J. L. Burch (2021), Mms observations of the multiscale wave structures and parallel electron heating in the vicinity of the southern exterior cusp, *Journal of Geophysical Research: Space Physics*, *126*(3), doi:10.1029/2019JA027698.

Otto, A. (1990), 3D resistive MHD computations of magnetospheric physics, *Computer Physics Communtications*, *59*, 185–195.

Otto, A., and D. H. Fairfield (2000), Kelvin-Helmholtz instability at the magnetotail boundary: MHD simulation and comparison with Geotail observations, *Journal of Geophysical Research*, *105*, 21,175–21,190.

Paschmann, G., B. O. . Sonnerup, I. Papamastorakis, G. Haerendel, S. J. Bame, J. R. Asbridge, J. T. Gosling, C. T. Russell, and R. C. Elphric (1979), Plasma acceleration at the Earth's magnetopause: evidence for reconnection, *Nature*, *282*, 243–246.

Pollock, C., T. Moore, A. Jacques, J. Burch, U. Gliese, Y. Saito, T. Omoto, L. Avanov, A. Barrie, V. Coffey, J. Dorelli, D. Gershman, B. Giles, T. Rosnack, C. Salo, S. Yokota, M. Adrian, C. Aoustin, C. Auletti, S. Aung, V. Bigio, N. Cao, M. Chandler, D. Chornay, K. Christian, G. Clark, G. Collinson, T. Corris, A. D. L. Santos, R. Devlin, T. Diaz, T. Dickerson, C. Dickson, A. Diekmann, F. Diggs, C. Duncan, A. Figueroa-Vinas, C. Firman, M. Freeman, N. Galassi, K. Garcia, G. Goodhart, D. Guererro, J. Hageman, J. Hanley, E. Hemminger, M. Holland, M. Hutchins, T. James, W. Jones, S. Kreisler, J. Kujawaski, V. Lavu, J. Lobell, E. LeCompte, A. Lukemire, E. MacDonald, A. Mariano, T. Mukai, K. Narayanan, Q. Nguyan, M. Onizuka, W. Paterson, S. Persyn, B. Piepgrass, F. Cheey, A. Rager, T. Raghuram, A. Ramil, L. Reichenthal, H. Rodriguez, J. Rouzaud, A. Rucker, Y. Saito, M. Samara, J.-A. Sauvaud, D. Schuster, M. Shappirio, K. Shelton, D. Sher, D. Smith, K. Smith, S. Smith, D. Steinfeld, R. Szymkiewicz, K. Tanimoto, J. Taylor, C. Tucker, K. Tull, A. Uhl, J. Vloet, P. Walpole, S. Weidner, D. White, G. Winkert, P.-S. Yeh, and M. Zeuch (2016), Fast plasma investigation for Magnetospheric Multiscale, *Space Science Reviews*, *199*, 331–406, doi:10.1007/s11214-016-0245-4.

Potter, D. (1973), *Computational Physics*, John Wiley and Sons.

Russell, C. T., B. J. Anderson, W. Baumjohann, K. R. Bromund, D. Dearborn, D. Fischer, G. Le, H. K. Leinweber, D. Lenema, W. Magnes, J. D. Means, M. B. Moldwin, R. Nakamura, D. Pierce, F. Plaschke, K. M. Rowe, J. A. Slavin, R. J. Strangeway, R. Torbet, C. Hagen, I. Jernej, A. Valavanoglou, and I. Ricter (2016), The Magnetospheric Multiscale magnetometers, *Space Science Reviews*, *199*, 189–256, doi:10.1007/s11214-014-0057-3.

Sonnerup, B. U. O., and M. Scheible (1998), *Analysis Methods for Multi-Spacecraft Data*, chap. Minimum and Maximum Variance Analysis, pp. 185–220, International Space Science Institute.

Sonnerup, B. U. ., G. Paschmann, I. Papamastorakis, N. Sckopke, G. Haerendel, S. J. Bame, J. R. Asbridge, J. T. Gosling, and C. T. Russell (1981), Evidence for magnetic field reconnection at the Earth's magnetopause, *Journal of Geophysical Research: Space Physics*, *86*, doi:10.1029/JA086iA12p10049.

Sorathia, K. A., V. G. Merkin, A. Y. Ukhorskiy, R. C. Allen, K. Nykyri, and S. Wing (2019), Solar wind ion entry into the magnetosphere during northward IMF, *Journal of Geophysical Research: Space Physics*, *124*, doi: doi.org/10.1029/2019JA026728.

Stawarz, J. E., S. Eriksson, F. D. Wilder, R. E. Ergun, S. J. Schwartz, A. Pouquet, J. L. Burch, B. L. Giles, Y. Khotyaintsev, O. L. Contel, P.-A. Lindqvist, W. Magnes, C. J. Pollock, C. T. Russll, R. J. Strangeway, R. B. Torbert, L. A. Avanov, J. C. Dorelli, J. P. Eastwood, D. J. Gershman, K. A. Goodrich, D. M. Malaspina, G. T. Marklund, L. Mirioni, and A. P. Sturner (2016), Observations of turbulence in a Kelvin-Helmholtz event on 8 September 2015 by the Magnetospheric Multiscale mission, *Journal of Geophysical Research*, *121*, 11,021–11,034, doi:10.1002/10JA023458.

Taylor, M. G. G. T., B. Lavraud, C. P. Escoubet, S. E. Milan, K. Nykyri, M. W. Dunlop, J. A. Davies, R. H. W. Friedel, H. Frey, Y. V. Bogdanova, A. Asnes, H. Laasko, P. Trvincek, A. Masson, H. Opgenoorth, C. Vallat, A. N. Fazakerley, A. D. Lahiff, C. J. Owen, F. Pitout, Z. Pu, C. Shen, Q. G. Zong, H. Rme, J. Scudder, and T. L. Zhang (2008), The plasma sheet and boundary layers under northward IMF: a multi-point and multi-instrument perspective, *Advances in Space Research*, *41*, 1619–1629.

Taylor, M. G. G. T., H. Hasegawa, B. Lavraud, T. Phan, C. P. Escobet, M. W. Dunlop, Y. V. Bogdanova, A. L. Borg, M. Volwerk, J. Berchem, O. D. Constantinescu, J. P. Eastwood, A. Masson, H. Laakso, J. Soucek, A. N. Fazakerley, H. Frey, E. V. Panov, C. Shen, J. K. Shi, D. G. Sibeck, Z. Y. Pu, J. Wang, and J. A. Wild (2012), Spatial distribution of rolled up Kelvin-Helmholtz vortices at Earth's dayside and flank magnetopause, *Annales Geophysicae*, *30*, 1025–1035, doi:10.5194/angeo-30-1025-2012.

Torbet, R. B., C. T. Russell, w. Magnes, R. E. Ergun, P.-A. Lindqvist, O. LeContel, H. Vaith, J. Macri, S. Myers, D. Rau, J. Needell, B. King, M. Granoff, M. Chutter, I. Dors, G. Olsson, Y. V. Khotyaintsev, A. Eriksson, C. A. Kletzing, S. Bounds, B. Anderson, W. Baumjohann, M. Steller, K. Bromund, G. Le, R. Nakamura, R. J. Strangeway, H. K. Leinweber, S. Tucker, J. Westfell, D. Fisher, F. Plaschke, J. Porter, and K. Lappalainen (2016), The FIELDS instrument suite on MMS: scientific objectives, measurements, and data products, *Space Science Reviews*, *199*, 105–135, doi:10.1007/s11214=014-0109-8.

Wilder, F. D., R. E. Ergun, S. J. Schwartz, D. L. Newman, S. Eriksson, J. E. Stawarz, M. V. Goldman, K. A. Goodrich, D. J. Gershman, D. M. Malaspina, J. C. Holmes, A. P. Sturner, J. L. Burch, R. B. Torbert, P.-A. Lindqvist, G. T.

Marklund, Y. Khotyaintsev, R. J. Strangeway, C. T. Russel, C. J. Pollock, B. L. Giles, J. C. Dorelli, L. A. Avanov, W. R. Patterson, F. Plaschke, and W. Magnes (2016), Observations of large-amplitude, parallel, electrostatic waves associated with the Kelvin-Helmholtz instability by the Magnetospheric Multiscale mission, *Geophysical Research Letters*, *43*, 8859–8866, doi:10.1002/2016GL070404.

Wing, S., J. R. Johnson, P. T. Newell, and C.-I. Meng (2005), Dawn-dusk asymmetries, ion spectra, and sources in the northward interplanetary magnetic field plasma sheet, *Journal of Geophysical Research*, *110*, doi:10.1029//2005JA011086.

Zhao, C., C. T. Russell, R. J. Strangeway, S. M. Petrinec, W. R. Paterson, M. Zhou, B. J. Anderson, W. Baumjohann, K. R. Bromund, M. Chutter, D. Fischer, G. Le, R. Nakamura, F. Plaschke, J. A. Slavin, R. B. Torbert, and H. Y. Wei (2016), Force balance at the magnetopause determined with MMS: application to flux transfer events, *Geophysical Research Letters*, *43*, 11,941–11,947, doi: 10.1002/2016GL071568.

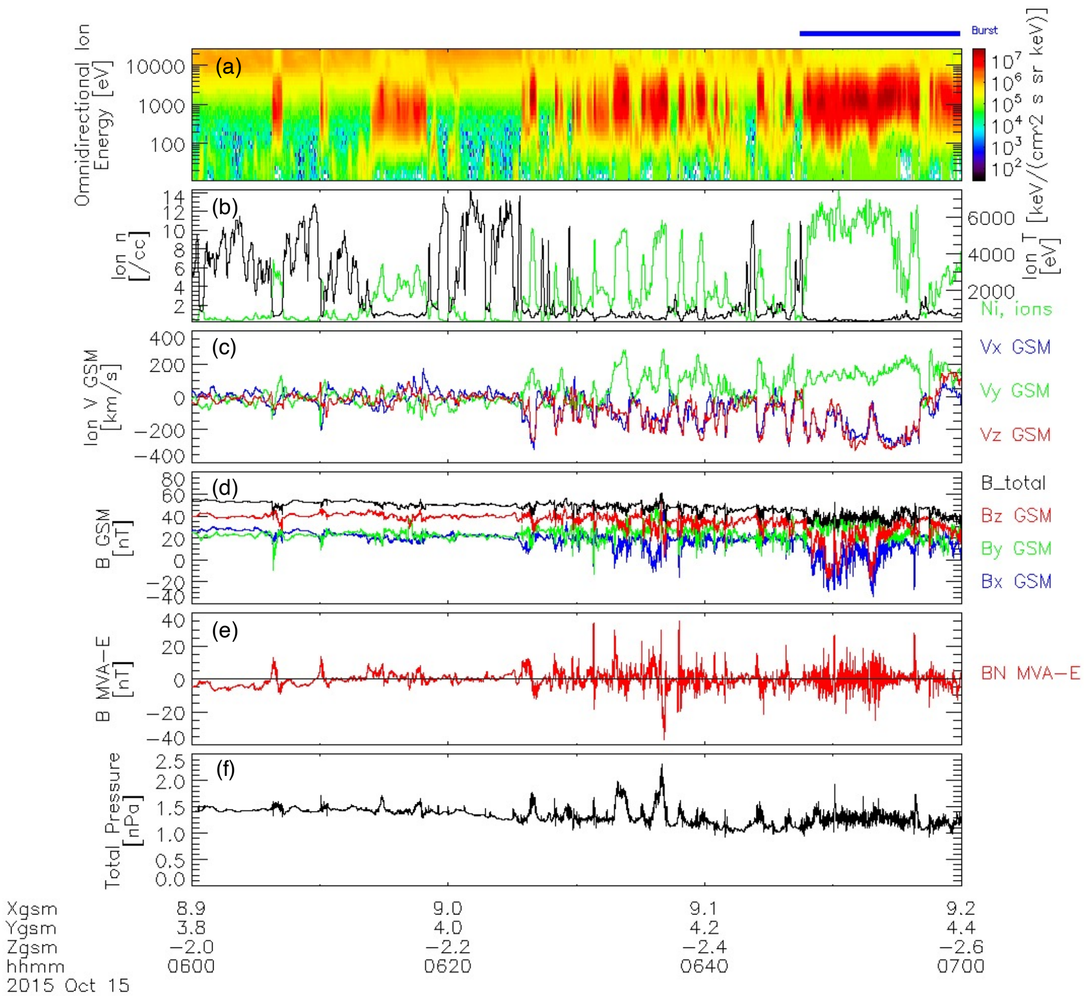

Figure 1. MMS observations of (a) omnidirectional ion energies; (b) ion density (green) and temperature (black); (c) ion bulk velocity in GSM coordinates; (d) direct current magnetic field in GSM coordinates; (e) the normal component of the magnetic field; and (f) total pressure from 06:00 to 07:00 UT on 15 October 2015. Ion data is taken from the Fast Plasma Investigation (FPI) and magnetic field data is from the Flux Gate Magnetometer (FGM) aboard MMS1. Burst mode data is available for the intervals marked in blue above the panels.

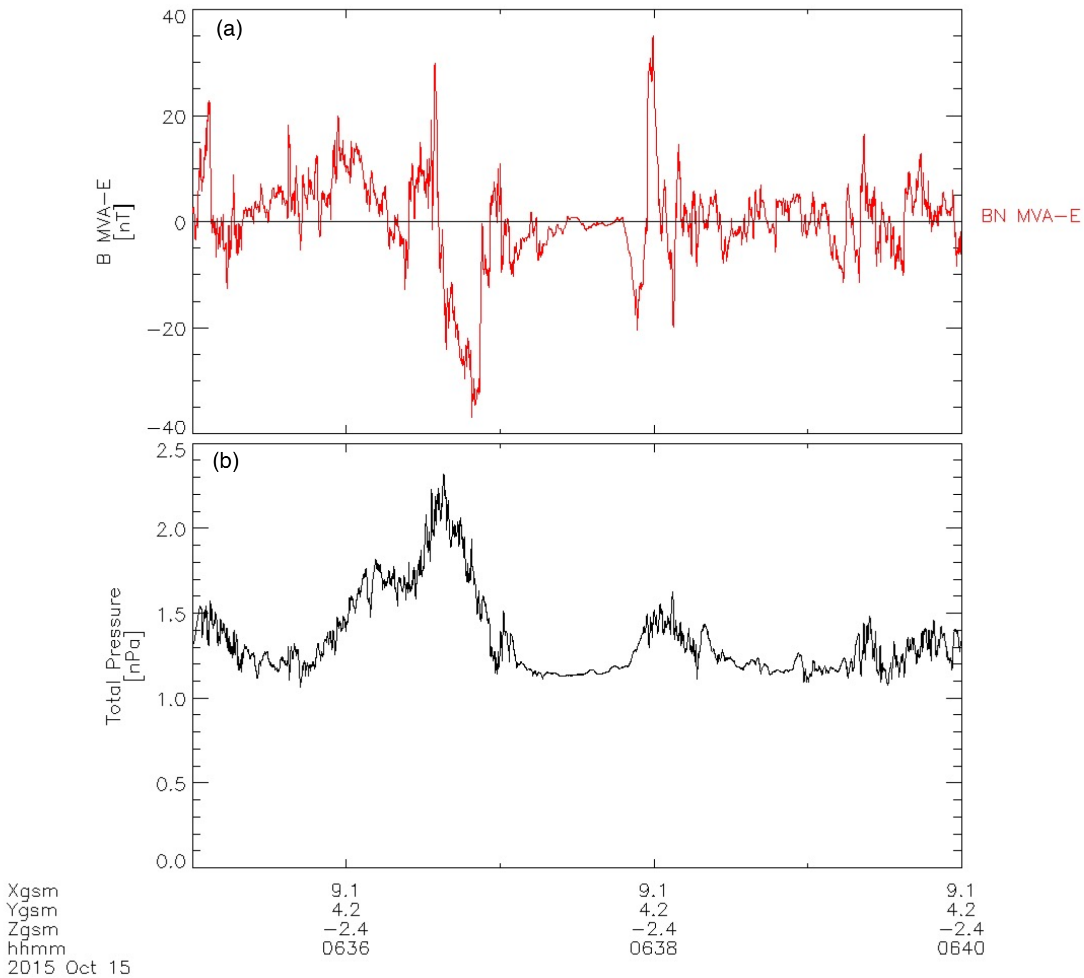

Figure 2. MMS1 observations of (a) the normal component of the magnetic field; and (b) total pressure from 06:35 to 06:40 UT on 15 October 2015. The magnetic field normal component is near 0 for approximately one minute at 6:37 UT, during which the total pressure is decreased indicating MMS is passing through the center of a KHI vortex.

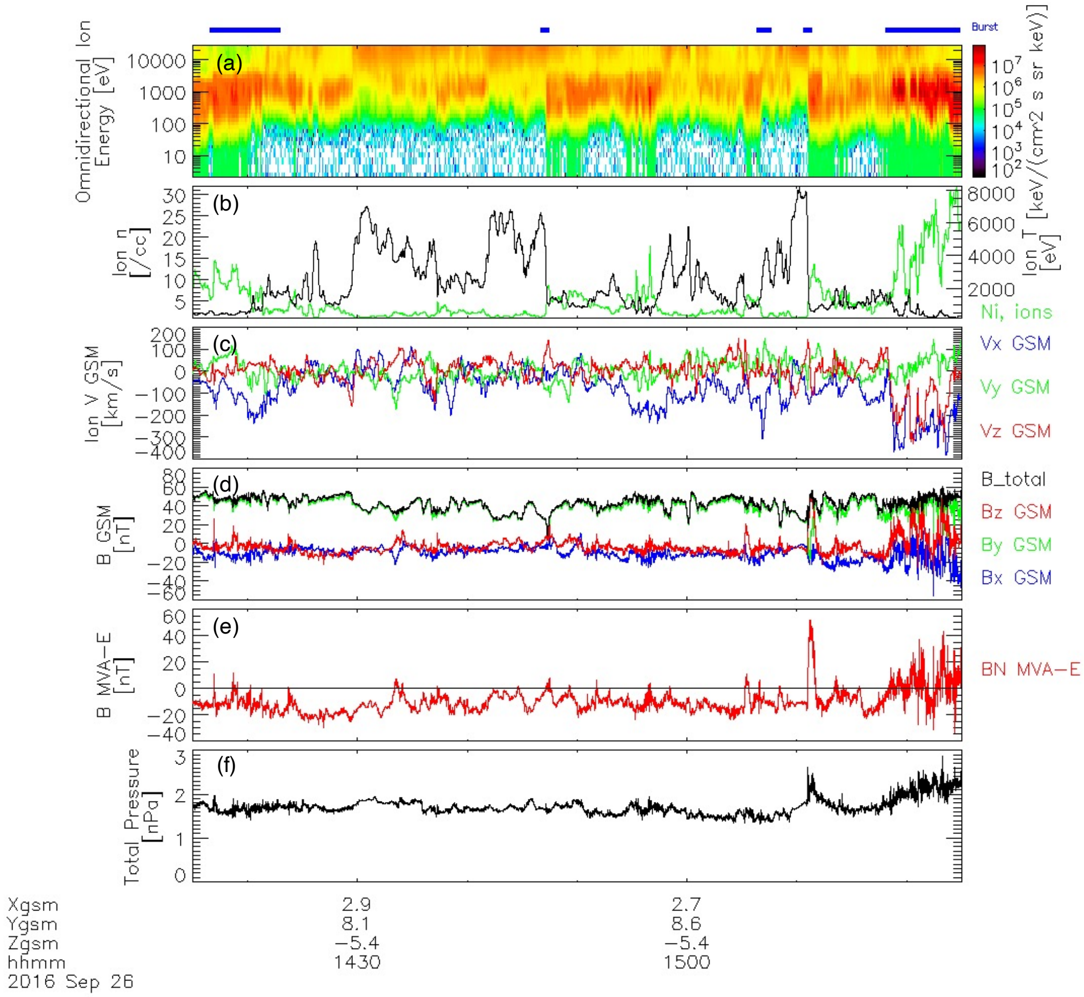

Figure 3. MMS observations as in Figure 1 from 14:15 to 15:25 UT on 26 September 2016. Ion data is taken from the Fast Plasma Investigation (FPI) and magnetic field data is from the Flux Gate Magnetometer (FGM) aboard MMS1. Bust mode data is available for the intervals marked in blue above the panels.

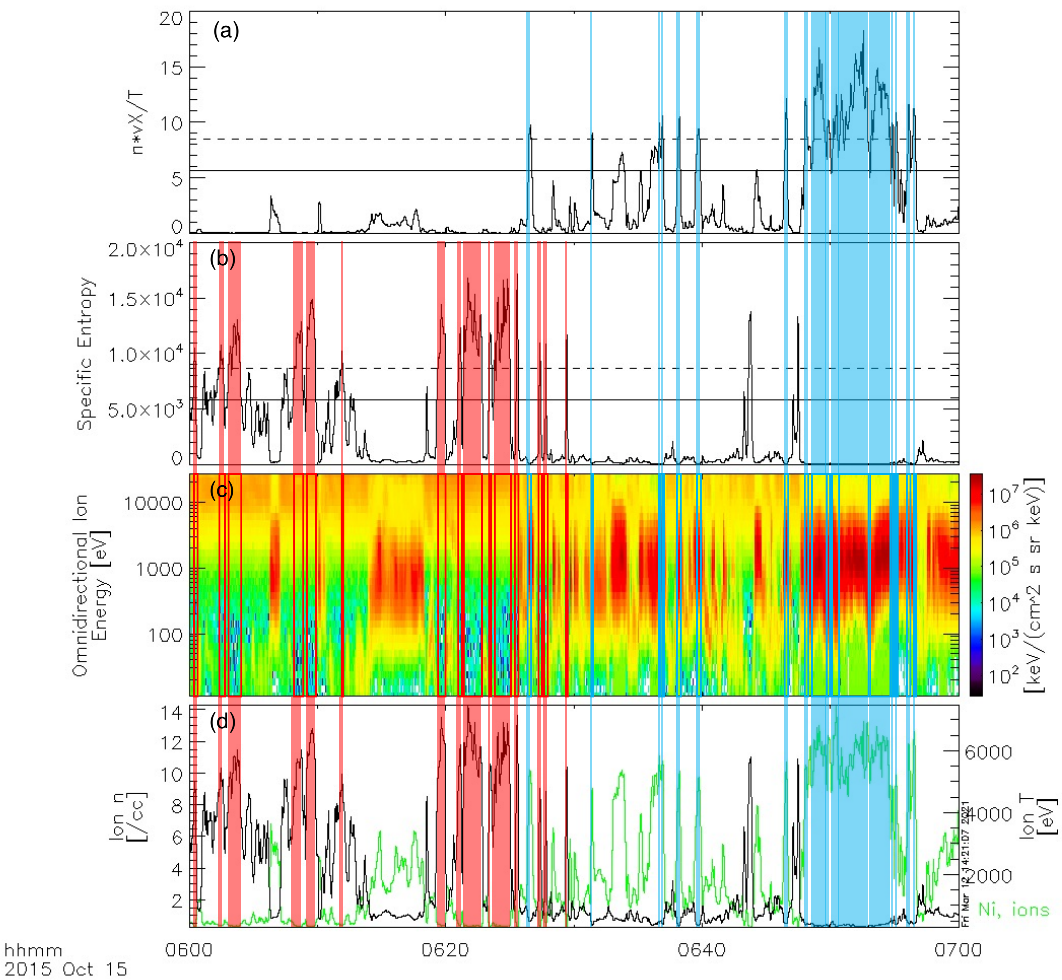

322 **Figure 4.** MMS observations of (a) the nv_{tail}/T parameter, and (b) specific entropy from
323 06:00 to 07:00 UT on 15 October 2016. The mean magnetopause value of each parameter and
324 the cutoff values for region identification are indicated by the solid and dashed lines respectively.
325 Blue (red) boxes indicate regions of magnetosheath (magnetospheric) plasma, which correspond
326 well with MMS observations of the (c) omnidirectional ion spectrogram and (d) ion density
327 (green) and temperature (black). Ion data is taken from the Fast Plasma Investigation (FPI)
328 aboard MMS1.

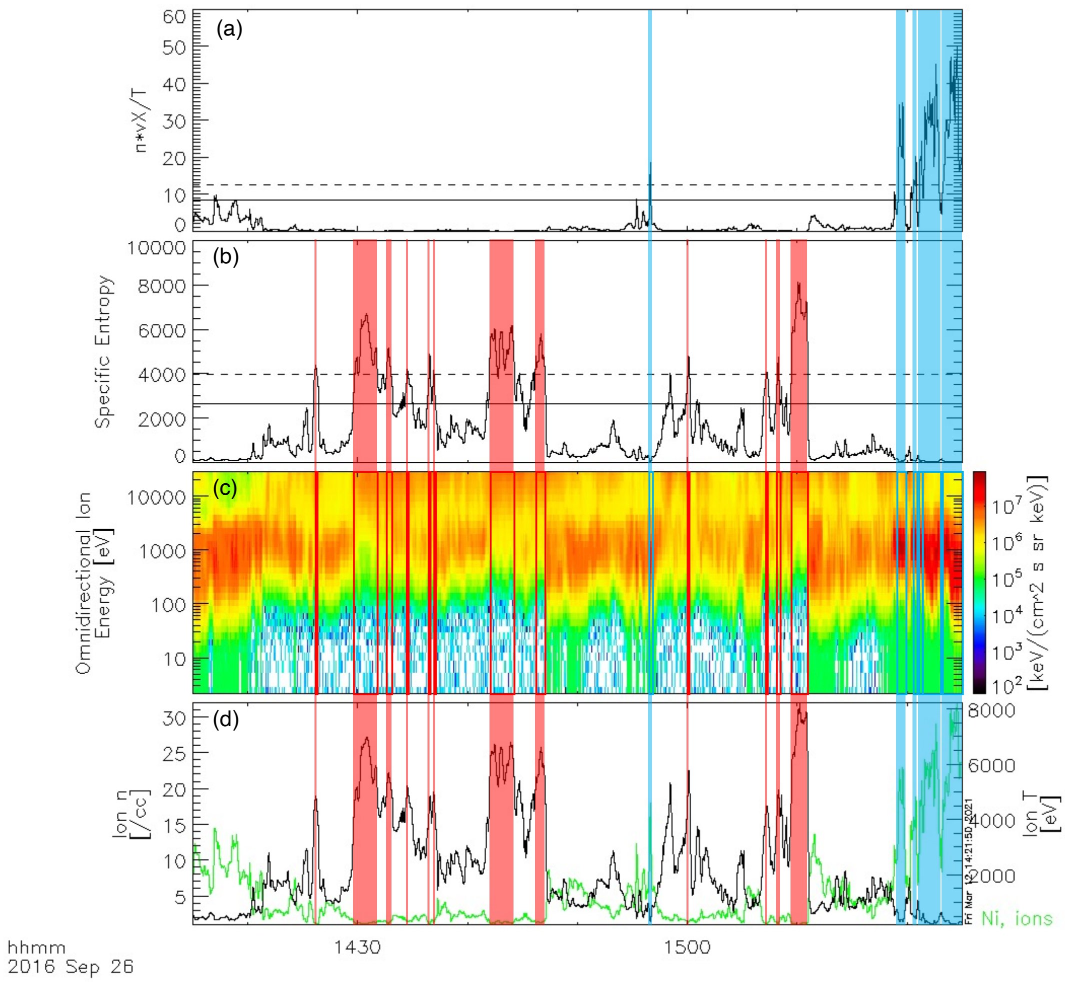

Figure 5. MMS observations as in Figure 4 from 14:15 to 15:25 UT on 26 September 2016. Ion data is taken from the Fast Plasma Investigation (FPI) aboard MMS1.

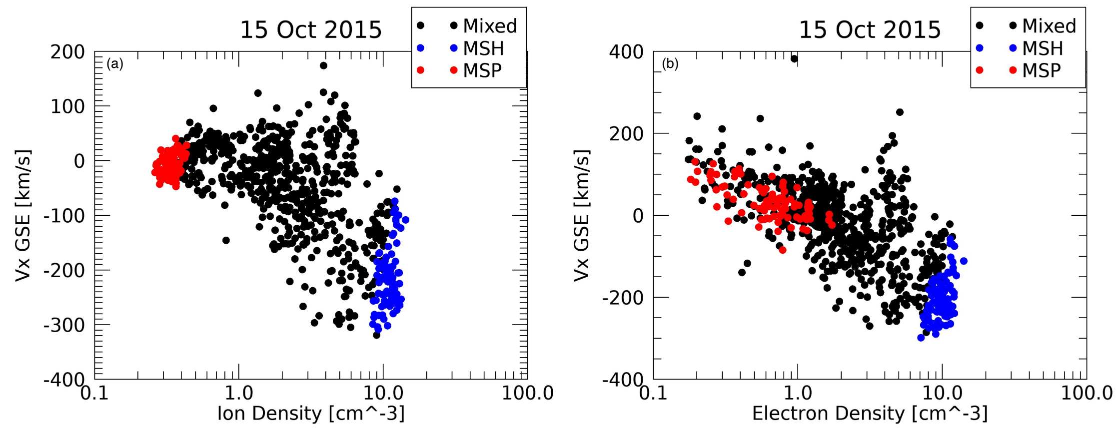

Figure 6. MMS observations of (left) tailward ion velocity as a function of ion density and (right) tailward electron velocity as a function of electron density for 06:00-07:00 on 15 October 2015. Blue (red) points were identified as magnetosheath (magntospheric) plasma. Mixed and ambiguous regions are plotted in black. In this case electrons show some evidence of roll-over within the KHI vortex: low density plasma typically associated with the magnetosphere is moving tailward with the faster magnetosheath plasma.

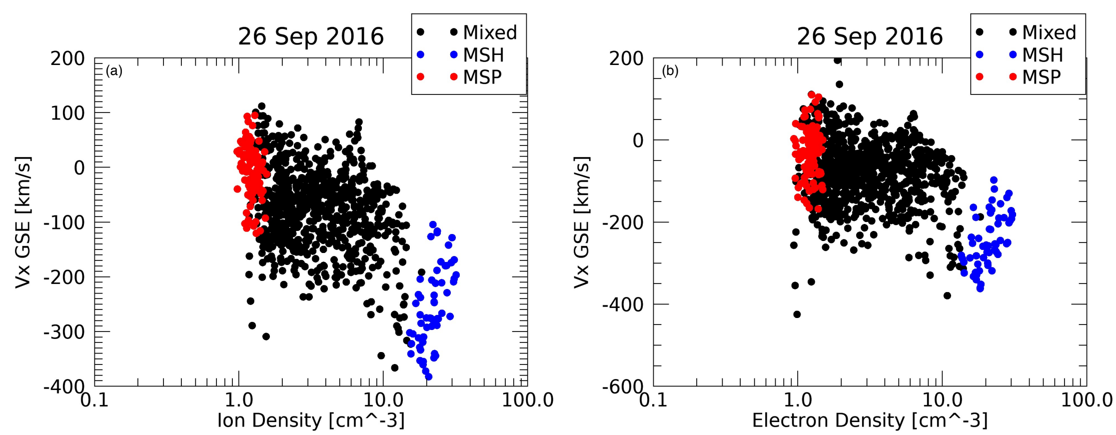

Figure 7. MMS observations as in Figure 6 for 14:15-15:25 on 26 September 2016. Blue, red, and black points represent plasma identified as the magnetosheath, magnetosphere, and mixed regions respectively. Both ions and electrons show evidence of roll-over within the KH vortex: some low density plasma typically associated with the magnetosphere is moving tailward with the faster magnetosheath plasma.

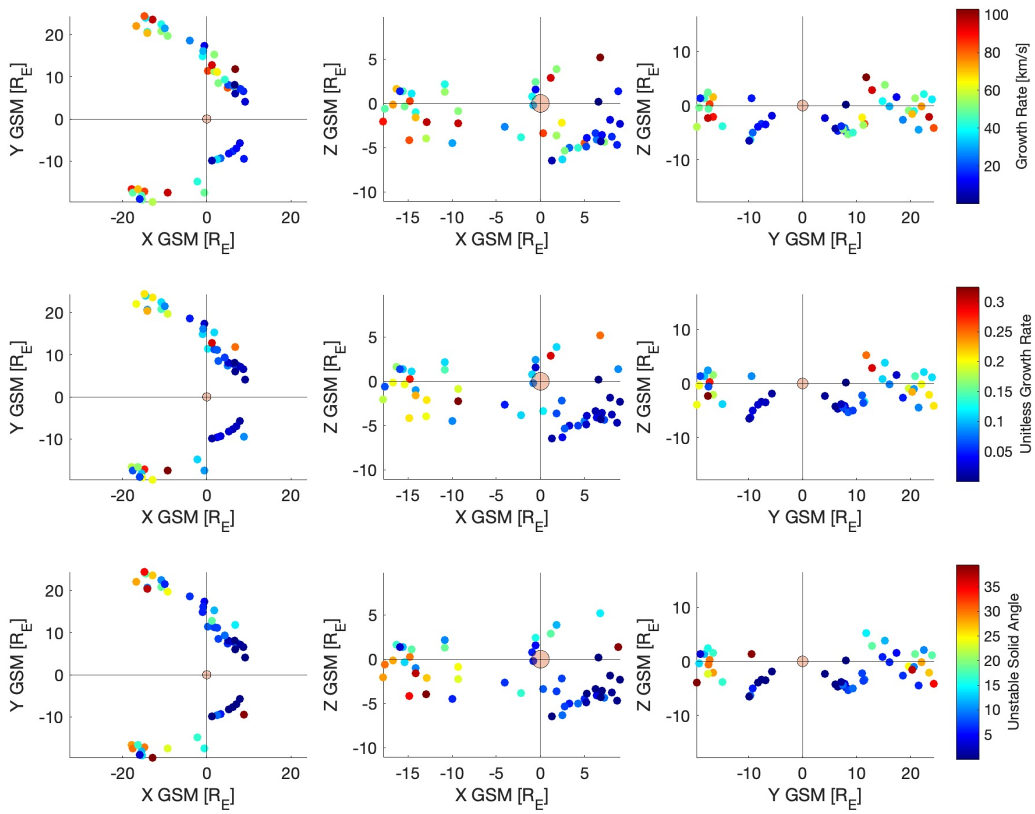

403 **Figure 8.** Growth rates (top row), unitless growth rates (middle row), and unstable solid
404 angles (bottom row) plotted with respect to the KHI's location along the magnetopause in GSM
405 X-Y plane (left column), X-Z plane (middle column), and Y-Z plane (right column).

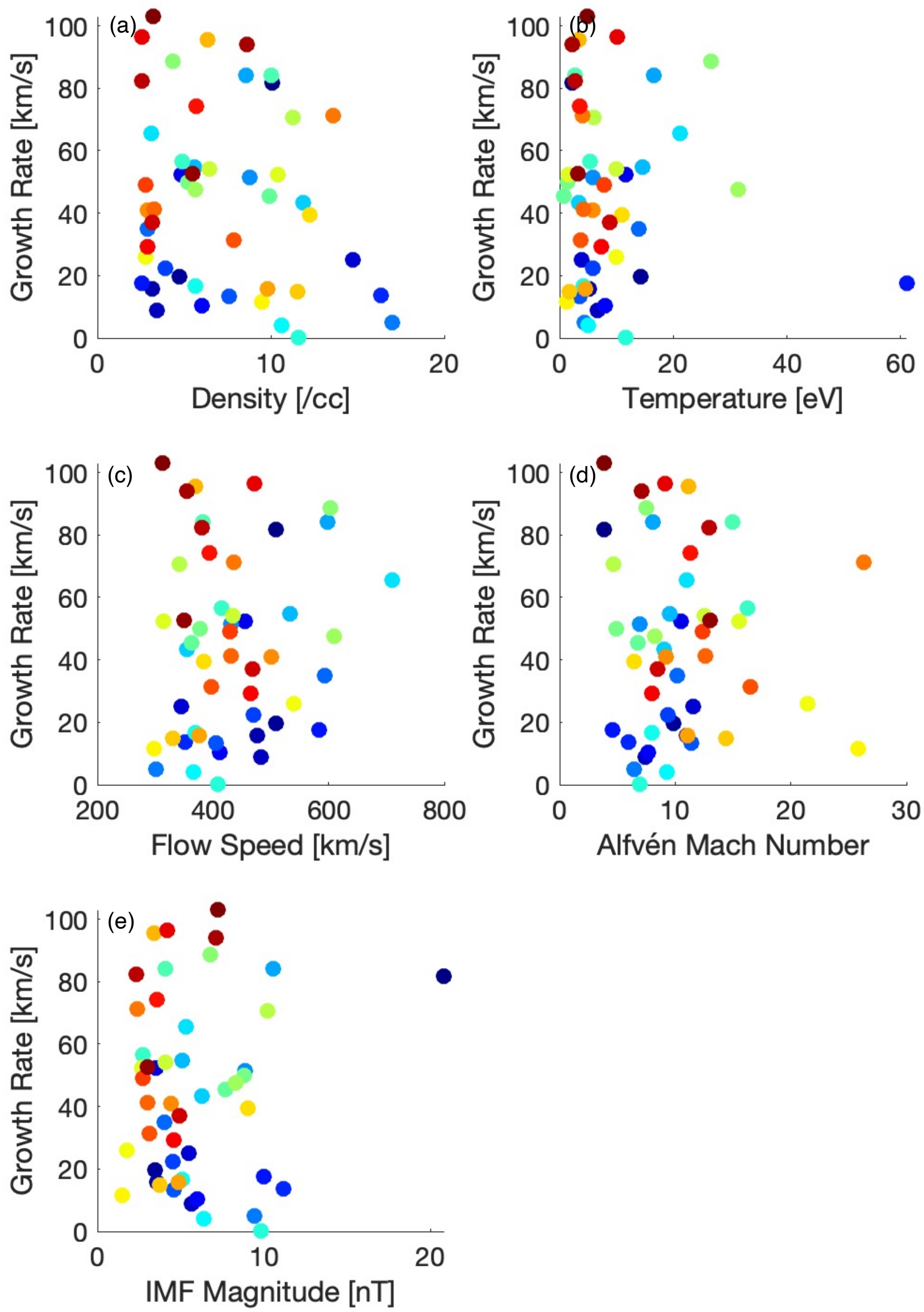

Figure 9. KHI growth rates as a function of solar wind (a) density, (b) temperature, (c) flow speed, (d) Alfvén mach number, and (e) average IMF magnitude. Other than a selection window from 295-610 km/s flow speed, growth rate is independent of solar wind parameters. Color indicates each unique event for comparison from plot to plot.

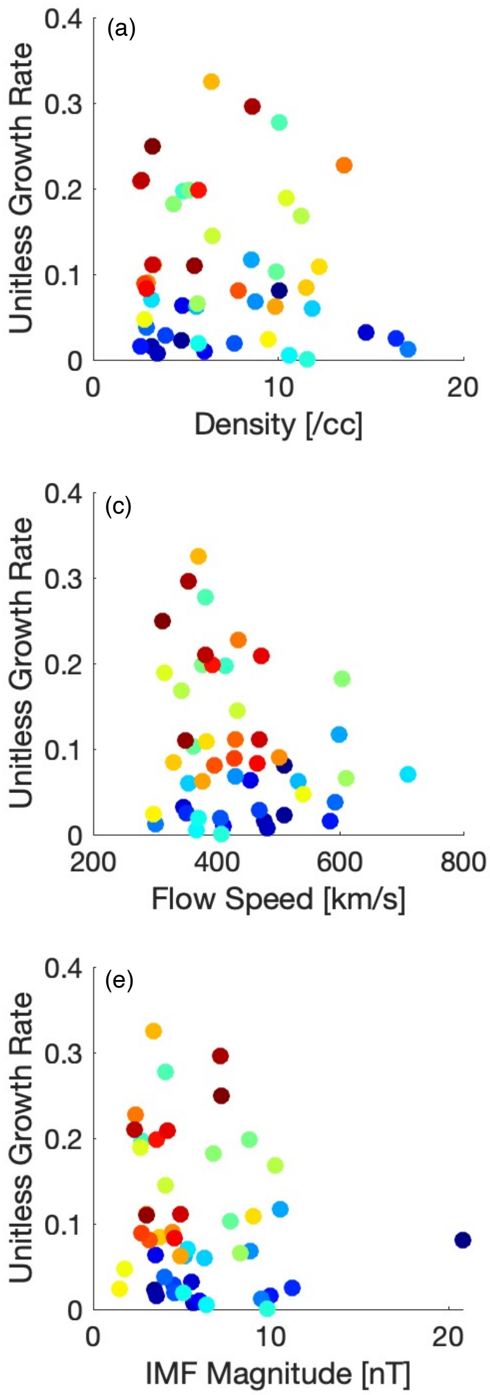

432 **Figure 10.** KHI unitless growth rates as a function of solar wind conditions as in Figure 9.
433 Other than a selection window from 295-610 km/s flow speed, growth rate is independent of solar
434 wind parameters. Color indicates each unique event for comparison from plot to plot.

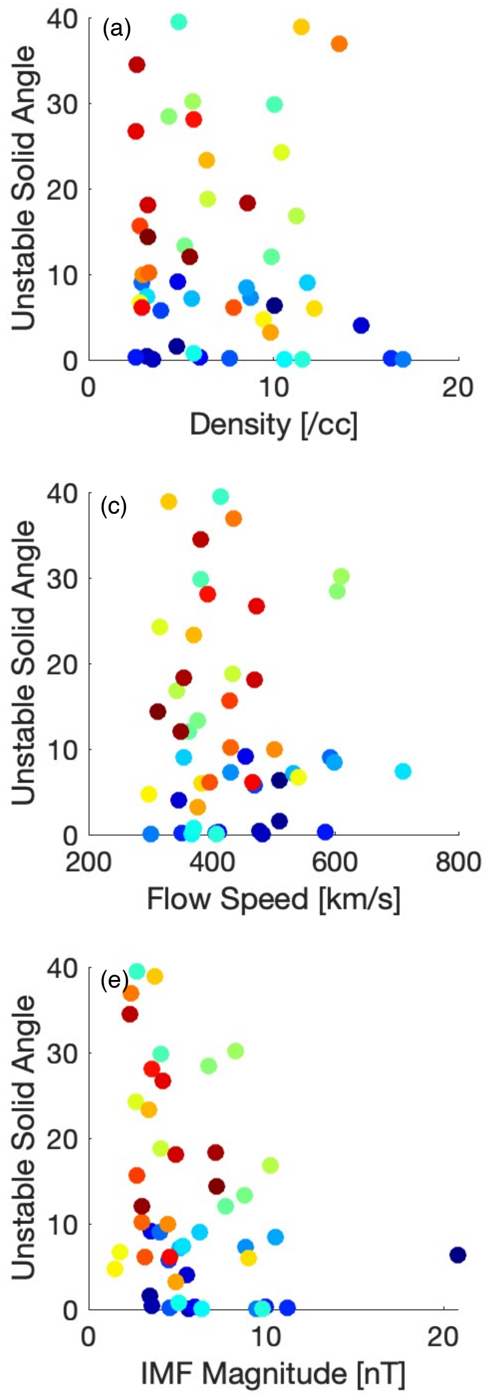

Figure 11. Unstable solid angles as a function of solar wind conditions as in Figure 9. Other than the selection window from 295-610 km/s flow speed, unstable solid angle is independent of solar wind parameters. Color indicates each unique event for comparison from plot to plot.

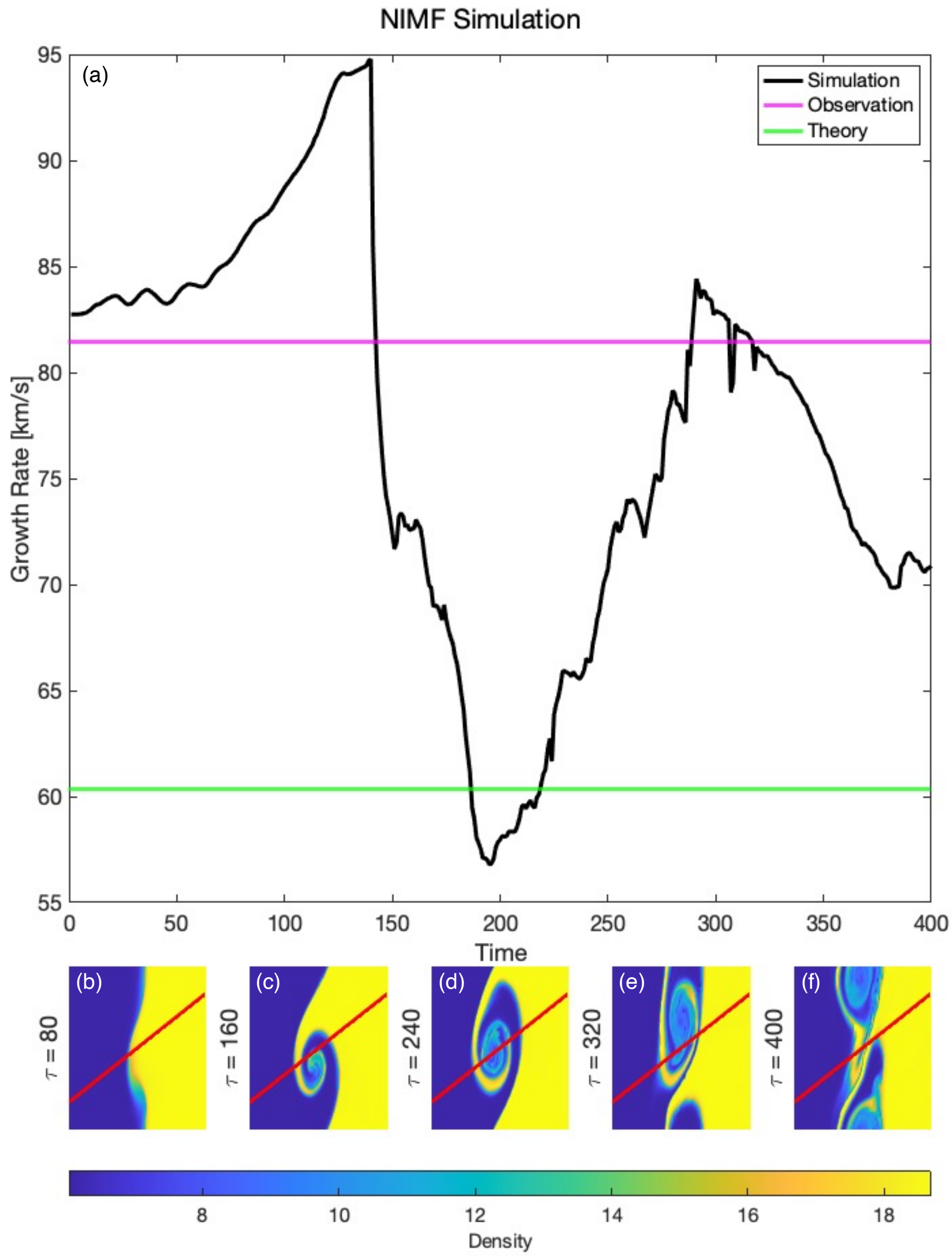

Figure 12. Growth rates were calculated and plotted as a function of time (a) using data from 2D MHD simulations of a dusk flank KHI occurring during Northward IMF. Initial conditions of the simulation are based on the event MMS observed on 08 September 2015. Density data from several time steps within the simulation (b)-(f) show the development of the KHI. Cuts, as indicated by the red line in panels (b)-(f), were taken through the instability at every simulation time step. The solid magenta line (a) indicates the growth rate for the MMS event on which the simulation is based. The green line (a) indicates the theoretical growth rate for the simulation as determined by the linear slope of $\ln(v_\perp)$ plotted as a function of time.

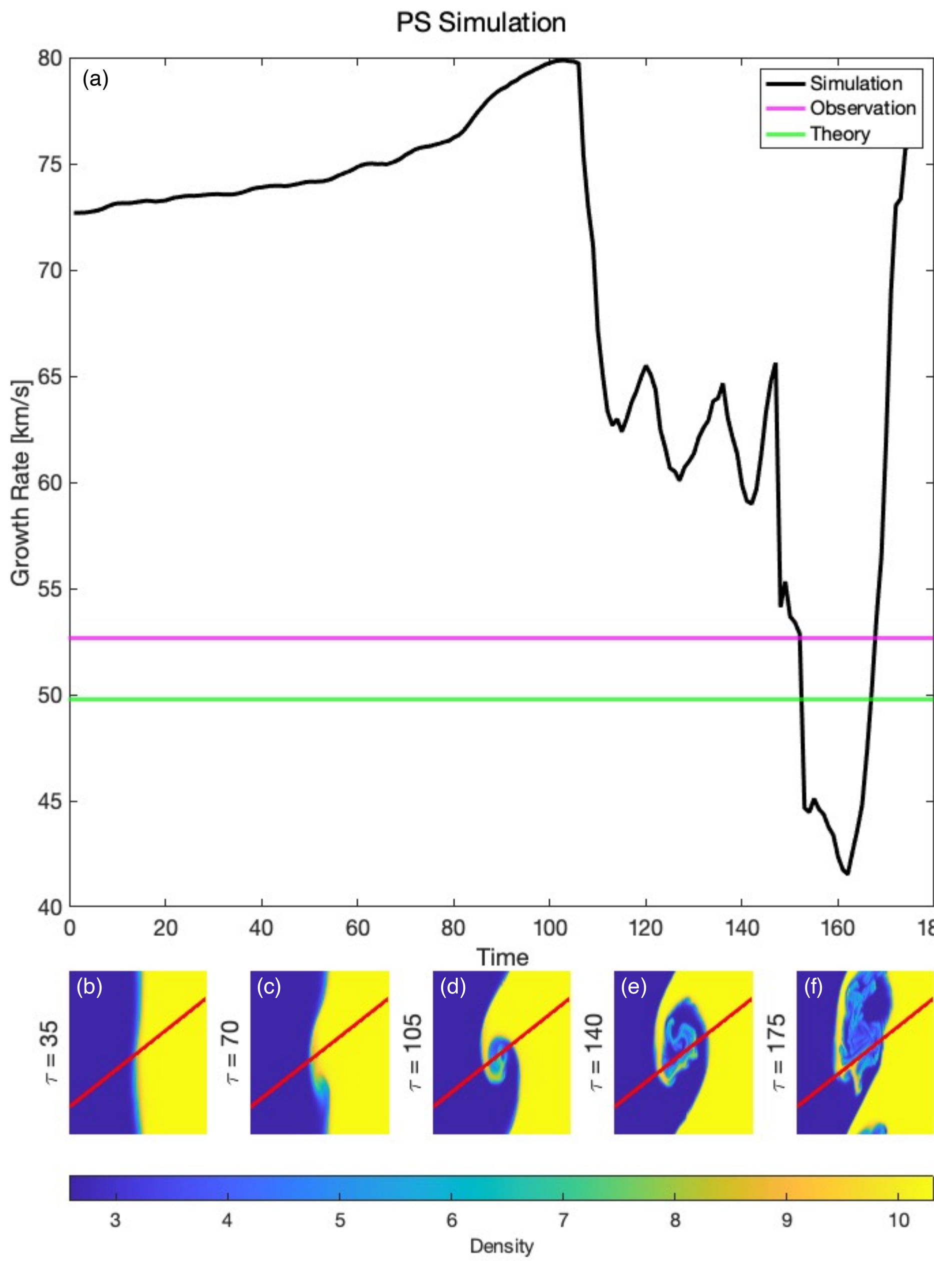

Figure 13. The KHI growth rates as in Figure 12 for a 2D MHD simulation of a dusk flank KHI occurring during Parker Spiral IMF orientation. Initial conditions of the simulation are based on the event MMS observed on 18 October 2015.